Formation of nanoripples on amorphous alumina thin films during low-energy ion-beam sputtering: Experiments and simulations

D. Babonneau,* E. Vandenhecke, and S. Camelio

Institut Pprime, Département Physique et Mécanique des Matériaux, UPR 3346 CNRS, Université de Poitiers, SP2MI, Téléport 2, 11 Bvd M. et P. Curie, BP 30179, 86962 Futuroscope Chasseneuil Cedex, France

(Received 15 July 2016; revised manuscript received 19 January 2017; published 9 February 2017)

The formation of nanopatterns induced by low-energy (0.5–1.5 keV) Xe^+ ion-beam sputtering of amorphous alumina thin films is investigated by atomic force microscopy and grazing incidence small-angle x-ray scattering. The observed dependence of the surface morphology on ion incidence angle, temperature, ion energy, and fluence is compared with the predictions of linear and nonlinear continuum theoretical models. The results show that ion-induced mass redistribution stabilizes the surface at near-normal and very grazing incidence angles, while curvature-dependent erosion governs the formation of periodic nanoripples in the range of incidence angles between 50° and 65°. Surface-confined ion-induced viscous flow is shown to be the dominant relaxation mechanism during erosion. Moreover, pattern evolution with ion fluence (pattern ordering and asymmetry of the ripple profile, in particular) suggests that nonlinear effects that are ignored by the Sigmund's collision cascade theory of sputtering contribute strongly to the observed dynamics of ripple formation.

DOI: 10.1103/PhysRevB.95.085412

I. INTRODUCTION

Low-energy ion-beam sputtering (IBS) of solid surfaces has recently attracted great interest as a flexible and competitive route for sublithographic patterning with a wide range of potential applications [1–3]. Indeed, IBS is known to generate ultrasmoothing or to produce a rich variety of nanoscale surface topographies through spontaneous self-organization processes. Depending on the processing conditions, namely ion-beam parameters (i.e., ion species, ion incidence angle, ion energy, ion flux, and fluence) as well as target composition and temperature, different surface features can emerge, such as one-dimensional (1D) ripple patterns or two-dimensional (2D) arrays of dots or holes, with typical size and spatial periodicity ranging from a few μm down to 10 nm. Because of its simplicity, versatility, and cost-effectiveness, IBS is hence considered to be a promising bottom-up approach to rapidly develop surface nanopatterns over macroscopic areas (up to several tens of cm^2 in just a few minutes) on a wide range of materials including metals [1,4], semiconductors [5–10], oxides [11–31], nitrides [16,17], ionic crystals [32,33], graphitelike or amorphous carbon [34,35], mica [36], pyrochlore [37], and even polymers [38,39].

Among the possible practical applications (e.g., in plasmonics [16,22,40,41], nanoscale bio-sensing [42,43], or magnetism [44–50]), ion-induced nanoripple patterns have recently become popular to be used as templates for growing conformal metallic thin films and self-aligned nanoparticles or nanowires with tailored functional properties resulting from anisotropic correlation phenomena. However, for these applications that crucially depend on the surface morphology and pattern quality, a precise experimental control as well as a full theoretical understanding of pattern formation is required. Building upon the pioneering work of Bradley and Harper in the late 1980s [51], significant theoretical effort has been expended and a number of theories for the ion-induced formation of ripple patterns have been advanced [52–61]. Generally, the time evolution of the surface topography during off-normal IBS and the spontaneous appearance (or not) of ordered 1D patterns is believed to be caused by a nontrivial competition between ion-induced destabilizing mechanisms (which roughen the surface) and stabilizing (smoothing) effects by different surface relaxation mechanisms. Although the understanding of the basic processes of pattern formation by IBS has recently evolved in important ways, it still constitutes a highly active research topic as no single model is able to give a consistent theoretical framework that encompasses all of the experimental findings. In particular, in view of the multiple physical mechanisms involved in the patterning dynamics, the essential question of identifying which effect is dominant remains open, thus stressing the need for further experimental and theoretical studies.

In the last decades, many studies dedicated to the formation of nanoripples by IBS have been performed on single as well as polycrystalline metals and semiconductor (groups IV and III-V) materials. On the contrary, studies with insulating oxide thin films are scarcer [11–19]. Moreover, although the morphological evolution of ion-induced ripple patterns has been investigated in detail in terms of ripple wavelength, ripple amplitude, and pattern ordering, there is no clear insight into the dependence of the ripple profile on the ion-beam parameters and target temperature. Also, the few experimental studies addressing this specific issue deliver partially contradictory results [12,23,25,28,36,42,62–67]. In this study we report on the evolution of the surface topography of amorphous alumina thin films exposed to a uniform Xe^+-ion beam in the low-energy range (0.5–1.5 keV). Atomic force microscopy (AFM) and grazing incidence small-angle x-ray scattering (GISAXS) experiments combined with a careful quantitative analysis are used to obtain accurate morphological characteristics of nanoripple patterns. The consistency of the experimental results (i.e., dependence of the surface morphology on ion incidence angle, temperature, ion energy, and fluence) with the predictions of linear and nonlinear continuum theoretical models is discussed. Our results evidence the possibility

*david.babonneau@univ-poitiers.fr

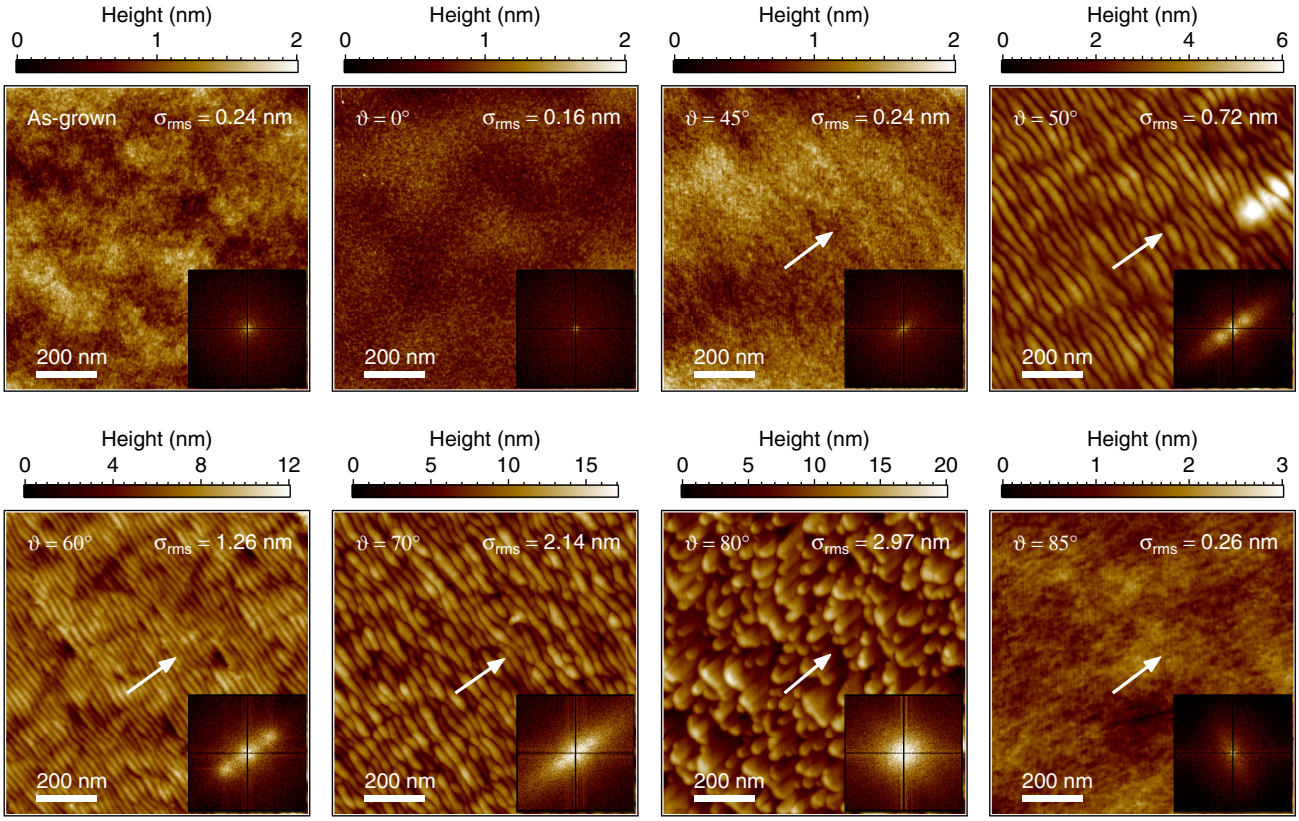

FIG. 1. AFM topographic images of amorphous alumina thin films before and after 1 keV Xe^+-ion exposure during 340 s with increasing ion incidence angles ϑ with respect to the surface normal ($T = 300$ K). Corresponding power spectral densities (PSD; squared modulus of the Fourier transform) of the images are shown in the inset and the projection of the ion-beam direction onto the surface is indicated by the white arrows.

to control by IBS the surface morphology of amorphous alumina at the nanoscale, but also confirm the complexity of formulating a holistic continuum model to describe the physical processes by which these surfaces self-organize.

II. EXPERIMENTAL DETAILS

A. Production and ion erosion of alumina thin films

Deposition and ion erosion of amorphous alumina thin films were performed in a dual ion beam sputtering Nordiko™ chamber ($\sim 5 \times 10^{-8}$ mbar base pressure), as described in Ref. [16]. Alumina thin films totaling up to 450 nm in thickness were grown onto Si substrates, at normal incidence and at a rate of 0.15 nm s^{-1}, by IBS of an Al target while carrying out ion assistance by a 50 eV O_2^+ beam oriented at 45° with respect to the Si surface normal. The as-grown films typically had a mass density of 3.25 g cm^{-3} and their surface was smooth, with a root mean square (rms) roughness $\sigma_{rms} \approx 0.24$ nm (Fig. 1). Ion erosion of the as-grown films was carried out with a collimated Xe^+-ion beam (beam diameter ~100 mm) produced from a filamentless radio-frequency ion source. The ion current was kept constant at 40 mA cm^{-2} corresponding to a nominal ion flux of about 3×10^{15} ions cm^{-2} s^{-1}. The ion incidence angle ϑ was varied between 0° and 85° with respect to the surface normal, and the temperature T was adjusted from 300 to 873 K by heating the sample holder with a lamp furnace. The ion gun was operated at ion energies E ranging from 0.5 to 1.5 keV, and the erosion time was varied between 90 and 1200 s. The thickness of the alumina thin films was characterized before and after Xe^+-ion exposure by spectroscopic ellipsometry measurements, resulting in an accurate determination of the erosion rate v_0. Representative variations of v_0 with different operating conditions are reported in Table I, as well as the corresponding fluences ϕ determined from TRIDYN [68] calculations. For a given erosion time of 340 s (i.e., for a given nominal fluence of about 10^{18} ions cm^{-2}), it can be observed a decrease of the estimated total fluence ϕ (and indeed of the effective flux F_{eff}) with ϑ and E that may result from nonuniformity of the ion beam and change of the beam divergence with E.

B. Morphological characterization of ion-eroded alumina thin films

The surface topography of alumina thin films was characterized at a local scale before and after Xe^+-ion exposure by AFM with a MultiMode equipment (Digital Instruments) operated in the tapping mode under ambient conditions and using silicon tips with a nominal radius of curvature of ~12–16 nm. In order to get statistical information averaged over macroscopic dimensions, ion-eroded alumina thin films were also analyzed by GISAXS 3D mapping [17,70] performed at the European Synchrotron Radiation Facility (Grenoble, France) with the

TABLE I. IBS of amorphous alumina thin films with Xe^+ ions during 340 s at room temperature: Variations of the erosion rate v_0 (from spectroscopic ellipsometry measurements) and total fluence ϕ (from TRIDYN [68] calculations) for different ion incidence angles ϑ and ion energies E. The ion range a, longitudinal straggling σ, and lateral straggling μ calculated using the Projected Range ALgorithm [69] are also given.

ϑ (deg)	E (keV)	v_0 (nm s^{-1})	ϕ (ions cm^{-2})	a (nm)	σ (nm)	μ (nm)
0	1.00	0.118	1.01×10^{18}	2.7	0.8	0.6
45	1.00	0.306	0.70×10^{18}	2.7	0.8	0.6
50	1.00	0.353	0.65×10^{18}	2.7	0.8	0.6
55	1.00	0.321	0.47×10^{18}	2.7	0.8	0.6
60	1.00	0.285	0.34×10^{18}	2.7	0.8	0.6
65	1.00	0.238	0.23×10^{18}	2.7	0.8	0.6
70	1.00	0.209	0.16×10^{18}	2.7	0.8	0.6
75	1.00	0.176	0.13×10^{18}	2.7	0.8	0.6
80	1.00	0.162	0.20×10^{18}	2.7	0.8	0.6
85	1.00	0.071	0.75×10^{18}	2.7	0.8	0.6
55	0.50	0.235	0.66×10^{18}	2.0	0.6	0.5
55	0.75	0.312	0.58×10^{18}	2.4	0.7	0.5
55	1.00	0.356	0.52×10^{18}	2.7	0.8	0.6
55	1.25	0.394	0.50×10^{18}	3.0	0.9	0.7
55	1.50	0.409	0.46×10^{18}	3.2	1.0	0.7

small-angle scattering setup of the D2AM beamline. The energy of the incident x-ray beam was fixed at 9.8 keV (radiation wavelength $\lambda = 0.1265$ nm) and the angle of incidence α_i with respect to the surface was close to the critical angle for total external reflection of alumina ($\alpha_c = 0.213^\circ$) in order to achieve high surface sensitivity. 2D GISAXS maps were measured as a function of the in-plane $2\theta_f$ and out-of-plane α_f exit angles with a 2D XPAD pixel detector located 1975 mm away from the sample. 3D mapping of the reciprocal space was accomplished by collecting series of $(2\theta_f,\alpha_f)$ GISAXS maps for different azimuth angles φ (i.e., the angle between the incident x-ray beam and the direction perpendicular to the projection of the ion beam onto the surface) starting from $\varphi = -15^\circ$ to $\varphi = 30^\circ$ by increments of 1°. The GISAXS intensity was analyzed within the distorted-wave Born approximation using the FITGISAXS package developed within the IGOR Pro software (WaveMetrics, Inc.) [71].

III. RESULTS

A. Dependence of ripple pattern with ion incidence angle

Figure 1 shows the angle dependence of the surface topography of alumina thin films exposed to a uniform 1 keV Xe^+-ion beam during 340 s at room temperature ($T = 300$ K). In agreement with previous observations made on 300 eV Ar^+-eroded alumina surfaces [29], IBS at normal incidence ($\vartheta = 0^\circ$) generates a smoothing of the initial surface whose rms roughness decreases below 0.2 nm. For off-normal incidence $\vartheta = 45^\circ$ and $\vartheta = 85^\circ$, the surface remains smooth and no discernible pattern emerges. We note that the absence of any surface nanopattern for incidence angles $\vartheta_c \leqslant 45^\circ$ is consistent with recent experimental studies of noble gas ion bombardment of impurity-free Si at room temperature [60,72]. However, although the existence of a critical angle for pattern formation has also been observed in the case of low-energy IBS of oxide surfaces like amorphous SiO_2 or crystalline Al_2O_3, smaller ϑ_c values in the range between 25° and 45° have been found in most cases [12,14,20–23,28,29]. For $50^\circ \leqslant \vartheta \leqslant 75^\circ$, IBS gives rise to periodic patterns consisting of unidirectional nanoripples with wave vector aligned parallel to the projection of the ion beam onto the surface [16,17,70]. In this ϑ range, the rms roughness increases dramatically from $\sigma_{rms} \approx 0.7$ nm at $\vartheta = 50^\circ$ to $\sigma_{rms} \approx 2.4$ nm at $\vartheta = 75^\circ$, while a minimum of period associated with a maximum of order is observed around $\vartheta = 60^\circ$. Furthermore, analysis of the slope angle distribution indicates that the ripple profile progressively changes from almost symmetric at $\vartheta = 50^\circ$ to strongly asymmetric with increasing ion incidence angle, so that the side facing the ion beam is steeper than the opposite side (see the Supplemental Material, Fig. S1 [73]). Finally, in a narrow angular range around $\vartheta = 80^\circ$, irregular and rough surfaces ($\sigma_{rms} \approx 3$ nm) are produced with roof-tile structures elongated along the ion beam, as already observed in previous grazing incidence experiments on monoelemental materials [66,67,74], as well as on SiO_2 [14,20,21] or on Al_2O_3 [28] surfaces bombarded by Ar^+ ions. The development of such structures elongated along the beam direction is frequently ascribed to geometric shadowing effects or to sputtering of the upwind faces by ions reflected on the downwind faces (Hauffe mechanism [75]).

Experimental 2D GISAXS patterns $(2\theta_f,\alpha_f)$ taken at $\varphi = 0^\circ$ for ion incidence angles in the range from $\vartheta = 50^\circ$ to 65° are displayed in Fig. 2 (top panel). The development of periodic ripple patterns is corroborated by the presence of two clearly separated side streaks, whose $2\theta_f$ position and α_f extension are very sensitive to the ion incidence angle. In agreement with AFM characterizations, an increasing asymmetry in the intensity distribution with respect to $2\theta_f = 0^\circ$ is also observed. The corresponding experimental in-plane GISAXS maps $(2\theta_f,\varphi)$ obtained at $\alpha_i + \alpha_f = 0.5^\circ$ are displayed in Fig. 2 (bottom panel), which exhibits elongated spots centered at $\varphi \approx 0^\circ$ with an azimuthal distribution $\Delta\varphi$ strongly dependent on ϑ. These results unambiguously confirm that the nanoripples created in this ϑ range are oriented perpendicular to the projection of the ion beam on the whole surface of the samples, but they possess various degrees of lateral order. Quantitative analysis of the GISAXS intensity distribution was performed following the model described in Refs. [17,70], while assuming straight ripples with the asymmetric sawtooth morphology schematized in Fig. 3(a). Corresponding simulated GISAXS patterns are presented in the Supplemental Material (Fig. S2) [73]. By increasing the ion incidence angle, the ripple wavelength Λ [Fig. 3(b)] initially decreases and then rises. Conversely, the pattern ordering characterized by the normalized ripple length L/Λ [Fig. 3(d)] and by the normalized lateral correlation length ξ/Λ [Fig. 3(e)] is first enhanced and then deteriorates with increasing ϑ. Ripples with the shortest wavelength ($\Lambda \approx 20$ nm) and best ordering ($L/\Lambda \approx 4$ and $\xi/\Lambda \approx 30$) are obtained at $\vartheta \sim 55^\circ$–60°. In parallel, consistently with AFM, the ripple height H increases almost linearly with ϑ [Fig. 3(c)], as well as the asymmetry of the ripple profile $\gamma_+ + \gamma_-$. Nevertheless, the slope of the upwind face $|\gamma_+|$ increases more rapidly than the slope of the downwind face $|\gamma_-|$, which actually evolves with a constant

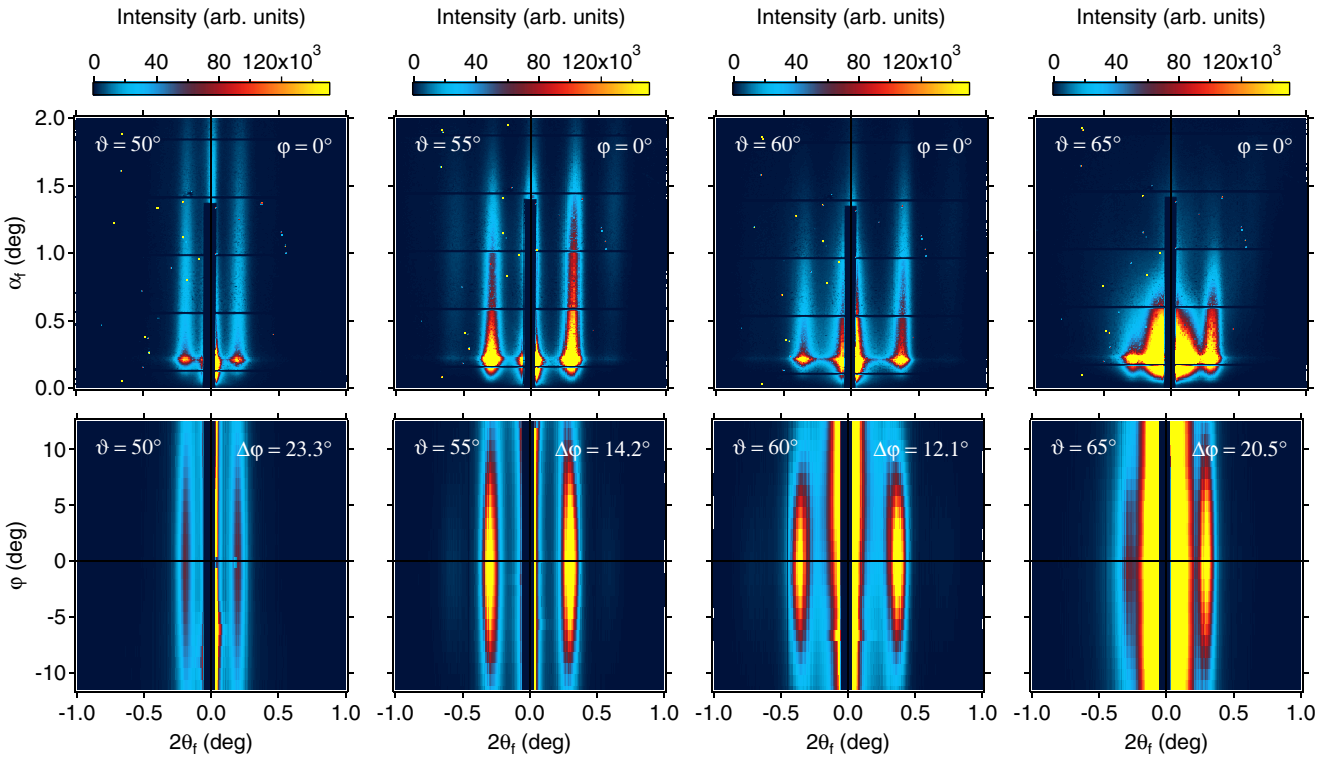

FIG. 2. GISAXS patterns of amorphous alumina thin films after 1 keV Xe^+-ion exposure during 340 s with increasing ion incidence angles ϑ with respect to the surface normal ($T = 300$ K). (Top panel) Experimental out-of-plane ($2\theta_f$,α_f) maps at $\varphi = 0°$. (Bottom panel) In-plane ($2\theta_f$,φ) maps at $\alpha_i + \alpha_f = 0.5°$. $\Delta\varphi$ is the azimuthal distribution of intensity, which is defined by the φ extension (full width at half maximum) of the ripple correlation peak.

value of about 22° for $\vartheta \geqslant 55°$ [Fig. 3(f)]. We note that the existence of such a "magic" downwind surface slope, independent of the ion-beam incidence angle ϑ, has also been observed by Engler *et al.* [67] after 2 keV Kr^+-ion exposure of Si(001) surfaces (with $|\gamma_-| \approx 8°$). To the best of our knowledge, there is still no explanation for this remarkable behavior. Moreover, in contrast to Ref. [67], we do not observe that the local incidence angle on the upwind face $\vartheta - \gamma_+$ remains concomitantly fixed [Fig. 10(a)].

B. Temperature dependence of ripple pattern

The temperature dependence of ripple patterns produced by 1 keV Xe^+ IBS of amorphous alumina thin films with $\vartheta = 55°$ and $\phi = 0.52 \times 10^{18}$ ions cm^{-2} ($F_{eff} = 1.54 \times 10^{15}$ ions $cm^{-2}\,s^{-1}$) was investigated by GISAXS 3D mapping (see the Supplemental Material, Figs. S3 and S4 [73]). Figure 4 gathers the main results collected from the quantitative analysis of the GISAXS data for applied temperatures $300 \leqslant T \leqslant 573$ K during IBS. In this temperature range, the formation of periodic ripple patterns with wave vector parallel to the projection of the ion beam onto the surface was routinely evidenced. However, the observed trends suggest that the ripple wavelength slightly increases with T [Fig. 4(a)], as already noticed in the case of SiO_2 or Al_2O_3 surfaces [12,28] eroded by low-energy Ar^+ ions incident at an angle of 45°. Concomitantly, the ripple height [Fig. 4(b)] as well as the pattern order [Fig. 4(c)] and profile asymmetry [Fig. 4(d)] decrease. It should be noted that in accordance with the gradual decrease of rms roughness and deterioration of ordering within the pattern, the surface morphology tends to become featureless and flat when T is further increased. Also, as observed by Zhou *et al.* [28], we found that thermal annealing at 873 K after IBS at $T = 300$ K did not produce any distinguishable modification of the nanorippled surface topography (not shown).

C. Ion energy dependence of ripple pattern

Figure 5 displays out-of-plane GISAXS maps taken at $\varphi = 0°$ for amorphous alumina thin films after Xe^+-ion exposure during 340 s at $T = 300$ K with $\vartheta = 55°$ and increasing ion energies E. The most visible impact is a progressive shift of the vertical scattering streaks toward smaller $|2\theta_f|$ values as E is raised. This indicates an increase of the ripple wavelength, which is consistent with most of the previous observations reported for ion-eroded amorphous or amorphizable surfaces in the low-energy range (i.e., $E < 2$–3 keV), including monoelemental [3,10,64] or oxide targets [12,14,20,28], and therefore suggests the need to consider nonthermal relaxation mechanisms to explain the dynamics of the ion-induced ripple patterns. Figure 6 shows the dependence of ripple morphology on ion energy obtained after quantitative analysis of the GISAXS data. Over the range $E = 0.5$ to 1.5 keV, we observe a power-law dependence of both the ripple wavelength [Fig. 6(a)] and height [Fig. 6(b)] such that $\Lambda \propto E^m$

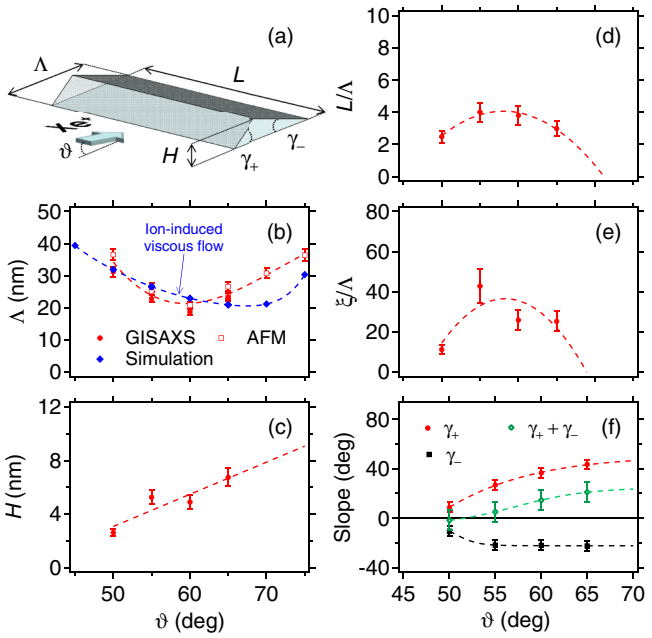

FIG. 3. (a) Schematic drawing of the ripple profile employed for GISAXS simulations. Morphological variations of nanoripples produced by 1 keV Xe^+ IBS of amorphous alumina thin films during 340 s as a function of the ion incidence angle ϑ with respect to the surface normal ($T = 300$ K): (b) ripple wavelength Λ, (c) ripple height H, (d) normalized ripple length L/Λ, (e) normalized lateral correlation length ξ/Λ, and (f) average slope γ_+ (γ_-) of the upwind (downwind) face. Dotted lines are guides to the eye.

and $H \propto E^n$ with $m = 0.58 \pm 0.02$ and $n = 0.35 \pm 0.02$, respectively. Simultaneously, within the uncertainty of the measurements, the pattern disorder [Fig. 6(c)] as well as the asymmetry of the ripple profile [Fig. 6(d)] are independent of E.

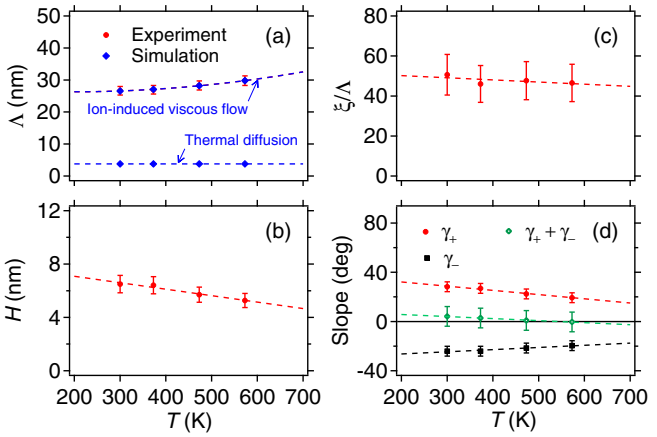

FIG. 4. Morphological variations of nanoripples produced by 1 keV Xe^+ IBS of amorphous alumina thin films as a function of the temperature T ($\phi = 0.52 \times 10^{18}$ ions cm^{-2} and $\vartheta = 55°$): (a) ripple wavelength Λ, (b) ripple height H, (c) normalized lateral correlation length ξ/Λ, and (d) average slope γ_+ (γ_-) of the upwind (downwind) face. Dotted lines are guides to the eye.

D. Pattern evolution with ion fluence

The time evolution of the surface topography of room temperature ion-eroded alumina thin films was also studied by GISAXS 3D mapping. Out-of-plane GISAXS maps taken at $\varphi = 0°$ for different ion fluences ϕ after 1 keV Xe^+ IBS with $\vartheta = 55°$ are shown in Fig. 7. A rapid coarsening of the ripple wavelength is evident from the shift of the vertical scattering streaks toward smaller $|2\theta_f|$ values. Furthermore, the narrowing of the first-order scattering streaks together with the progressive appearance of second-order streaks reveal the achievement of a higher degree of ordering at higher fluences. Regarding the evolution of the ripple profile, $(2\theta_f, \alpha_f)$ GISAXS maps exhibit a symmetric intensity distribution with respect to $2\theta_f = 0°$ at low fluences ($\phi \leqslant 1.39 \times 10^{17}$ ions cm^{-2}), whereas asymmetric scattering streaks characteristic of asymmetric ripples gradually develop at higher fluences. All these trends are confirmed in Fig. 8, which shows the dependence of ripple morphology on ion fluence deduced by GISAXS data fitting. In Fig. 8(a), the ripple wavelength is found to increase according to a power law $\Lambda \propto \phi^{0.15\pm0.01}$, although a certain tendency towards a saturation cannot be entirely ruled out. Similarly, the evolution of the ripple height is consistent with a power-law relationship $H \propto \phi^{0.10\pm0.01}$ [Fig. 8(b)], whereas the normalized lateral correlation length is increased from $\xi/\Lambda \approx 30$ at $\phi = 1.39 \times 10^{17}$ ions cm^{-2} to $\xi/\Lambda > 50$ at $\phi > 10^{18}$ ions cm^{-2}. In agreement with the ϕ dependence of Λ and H (i.e., $H/\Lambda \propto \phi^{-0.05}$), the average slope angles tend to drop when the ion fluence is increased. However, it can be also observed in Fig. 8(d) that the slope of the downwind face $|\gamma_-|$ decreases more rapidly than the slope of the upwind face $|\gamma_+|$, which results in the development of nanoripples with a gradual asymmetric shape. In previous studies of ripple formation by low-energy IBS of SiO_2 and Al_2O_3 surfaces, different dynamics corresponding to different regimes (i.e., linear or nonlinear) were reported. For example, in the case of IBS experiments performed at $\vartheta = 45°$, Umbach *et al.* [12] and Zhou *et al.* [28] found that the ripple wavelength remains nearly constant, whereas the ripple amplitude continues to increase with time. In contrast, evolution of the ripple wavelength and amplitude following power-law dependencies (with or without saturation at high fluences) were observed by other authors, but a number of different values of the exponent (between 0 and 1) were reported [15,20,21,26,27]. Also, at higher fluences, further evolution towards inhomogeneous and less ordered ripple patterns was observed by Keller *et al.* after 500 eV Ar^+ IBS of amorphous SiO_2 surfaces [14,15], which does not seem to be the case here. We note that no purely linear regime, where the ripple amplitude increases exponentially and the ripple wavelength stays constant, can be observed in the initial stage of the current experiments. This indicates that nonlinearities dominate the surface evolution even for the smallest ion fluences accessible with our experimental setup.

IV. DISCUSSION

Our results clearly show that periodic ripple patterns can be produced on amorphous alumina thin films during low-energy IBS for $50° \leqslant \vartheta \leqslant 75°$. In this ϑ range, the ripple wave vector is oriented uniformly in the direction parallel to the

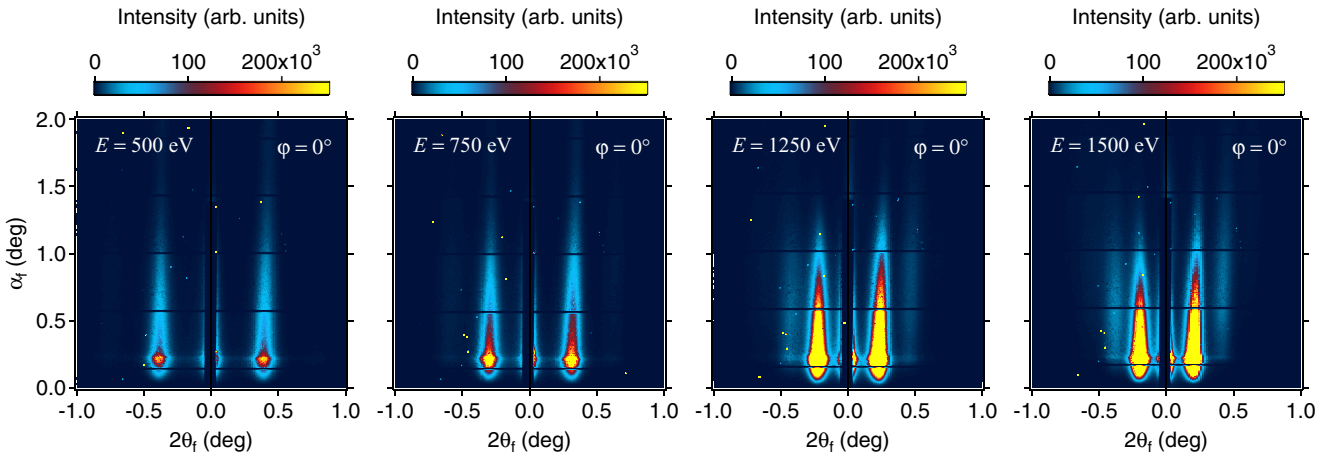

FIG. 5. Experimental 2D GISAXS patterns $(2\theta_f, \alpha_f)$ taken at $\varphi = 0°$ for amorphous alumina thin films after Xe^+-ion exposure during 340 s with increasing ion energies E ($\vartheta = 55°$ and $T = 300$ K).

projection of the ion beam onto the surface, which will be referred to as the x direction hereafter. In addition, both the ripple wavelength and ordering, but also the ripple height and profile display a strong dependence on the ion incidence angle (Sec. III A). Following the seminal work of Bradley and Harper [51], continuum models have been commonly employed to describe theoretically the formation of ripple and dot (or hole) patterns on surfaces subjected to IBS, with varying degrees of success. Originally it was proposed that periodic patterns can emerge on the surface as a result of a delicate balance between curvature-dependent erosion (that tends to destabilize the surface) and surface relaxation by thermal diffusion (that induces smoothing) [51]. Later on, the linear Bradley-Harper's theory has been generalized to include nonlinear and noise terms [52,76–78], which can modify the long term behavior of the surface dynamics (e.g., height saturation, profile asymmetry, kinetic roughening, etc.). More sophisticated models, which exploits the coupling between

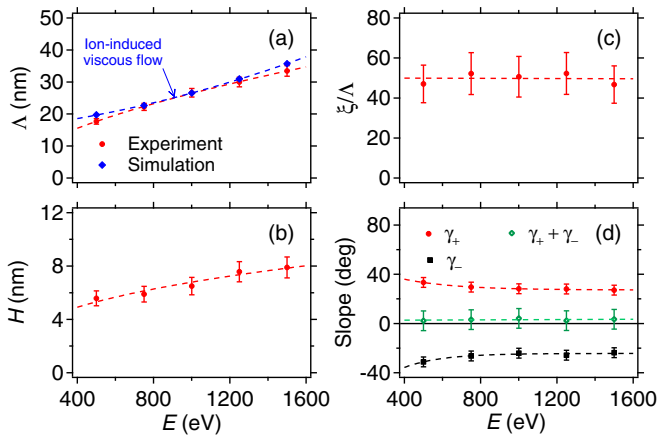

FIG. 6. Morphological variations of nanoripples produced by Xe^+ IBS of amorphous alumina thin films during 340 s as a function of the ion energy E ($\vartheta = 55°$ and $T = 300$ K): (a) ripple wavelength Λ, (b) ripple height H, (c) normalized lateral correlation length ξ/Λ, and (d) average slope γ_+ (γ_-) of the upwind (downwind) face. Dotted lines are guides to the eye.

the surface topography and a thin surface layer with altered viscosity [53,79] or composition [54,55], have been recently advanced to account for usual experimental observations such as wavelength coarsening and enhancement of pattern ordering. Furthermore, the need to consider alternative (nonthermal) relaxation mechanisms, such as ion-induced effective surface diffusion [52,77], surface-confined ion-induced viscous flow [12,28], ion-induced stress [56,57,80–82], or stress-induced mass transportation [83,84], has been established. The possible contribution of ion-induced mass redistribution (curvature-dependent ballistic drift), which causes stabilization of the surface at near-normal ion incidence angles and becomes unstable for $\vartheta > 45°$, has also been identified to play a critical role in the surface evolution as an additional mechanism competing with curvature-dependent erosion [58–61]. In the following sections, in order to elucidate the relevant processes involved in the formation of nanoripple patterns during Xe^+ IBS of amorphous alumina thin films, our experimental results for films exposed to a uniform ion beam during 340 s are first discussed on the basis of linear continuum models. Indeed, even though nonlinear effects contribute to the formation of the ripple patterns, such a straightforward approach has been proven effective for serving as a basis for predicting the angular regions where ripple formation can be expected and for enabling the contribution of various roughening and smoothing mechanisms to be separated [12,28,29,35,85]. Next, the patterning dynamics (erosion time between 100 and 1256 s) is compared to numerical integrations of nonlinear differential equations, which are more time consuming, but more appropriate and more accurate to describe the morphology of ion-induced ripple patterns and their evolution in the high-fluence regime.

A. Linear continuum models

1. *Instability mechanism: Effects of curvature-dependent erosion and mass redistribution*

An expansion formula of the linear continuum equation derived by Bradley and Harper [51] with fourth-order derivatives [77] to describe the time evolution of the surface profile

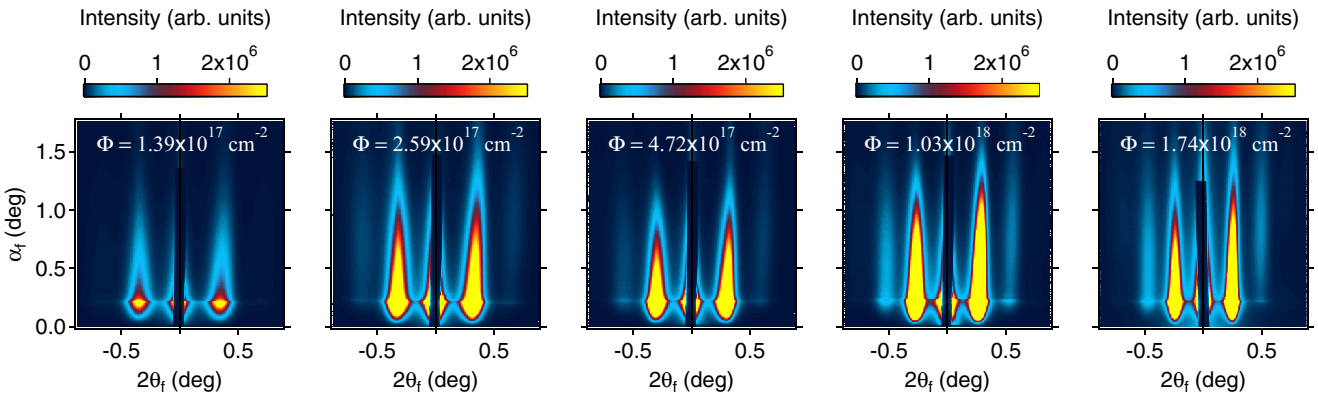

FIG. 7. Experimental 2D GISAXS patterns $(2\theta_f,\alpha_f)$ taken at $\varphi = 0^\circ$ for amorphous alumina thin films after 1 keV Xe^+-ion exposure with increasing ion fluences ϕ ($\vartheta = 55^\circ$ and $T = 300$ K).

$h(x,y,t)$ during IBS is given by

$$\frac{\partial h}{\partial t} = -v_0 + \gamma_x \frac{\partial h}{\partial x} + \nu_x \frac{\partial^2 h}{\partial x^2} + \nu_y \frac{\partial^2 h}{\partial y^2} - K_{xx} \frac{\partial^4 h}{\partial x^4} - K_{yy} \frac{\partial^4 h}{\partial y^4} - K_{xy} \frac{\partial^2 h}{\partial x^2} \frac{\partial^2 h}{\partial y^2} - \mathcal{K} \nabla^4 h, \quad (1)$$

where v_0 is the average erosion rate and γ_x is the dependence of the erosion rate on the local ion incidence angle, which causes a lateral motion of the surface pattern along the x direction. $\nu_x = \nu_x^{eros} + \nu_x^{redist}$ and $\nu_y = \nu_y^{eros} + \nu_y^{redist}$, which consist of the sum of an erosive contribution and a redistributive one, are curvature-dependent coefficients (often referred to as *effective surface tensions*) generating surface instability when negative. K_{xx}, K_{yy}, and K_{xy} correspond to the so-called ion-induced effective smoothing coefficients, which have a purely erosive origin unrelated to actual material transport [77]. The last term proportional to $\mathcal{K}$ describes additional surface relaxation mechanisms due to, e.g., thermal diffusion [86] or surface-confined ion-induced viscous flow [12], which are assumed to be isotropic. With the exception of $\mathcal{K}$, all coefficients in Eq. (1) are functions of IBS parameters v_0 and ϑ (see Table I) and of the Sigmund's parameters describing the spatial distribution of the deposited energy in the bombarded solid (i.e., the ion range a, longitudinal straggling σ, and lateral straggling μ), which can be roughly estimated using the Projected Range ALgorithm [69]. The corresponding relations are detailed in the Appendix [Eqs. (A1)–(A14)]. Equation (1), which can be solved by standard Fourier analysis, actually predicts that a smooth and stable surface morphology will be produced for positive values of ν_x and ν_y. Conversely, a single Fourier mode will dominate all the others for negative values of ν_x or ν_y, leading to the formation of periodic ripples with wave vector k_i ($i = x$ or y) oriented along the i direction and with a characteristic wavelength

$$\Lambda_i = \frac{2\pi}{k_i} = 2\pi \sqrt{\frac{2(K_{ii} + \mathcal{K})}{|\nu_i|}}, \quad (2)$$

where $i = x$ for $\nu_x < \nu_y$ and $i = y$ for $\nu_y < \nu_x$. Hence, the sign and relative magnitudes of the curvature-dependent coefficients control the absence or emergence of ion-induced ripple patterns as well as the ripple orientation.

In order to determine which instability mechanism (i.e., erosive or redistributive) dominates the formation of ripple patterns during Xe^+ IBS of amorphous alumina thin films, calculated values of $\nu_i^{eros}(\vartheta)$ [Eq. (A2)] and $\nu_i^{redist}(\vartheta)$ [Eqs. (A12) and (A13)] are shown in Figs. 9(b) and 9(c), respectively. The resulting $\nu_i(\vartheta) = \nu_i^{eros}(\vartheta) + \nu_i^{redist}(\vartheta)$ values are presented in Fig. 9(d). The prediction for the erosive contribution should results in the formation of parallel-mode ripples for $\vartheta \leqslant 71^\circ \pm 1^\circ$, whereas perpendicular-mode ripples should emerge for larger incidence angles. In contrast, the redistributive contribution should stabilize the surface below $\vartheta_c = 45^\circ$ and produce parallel-mode ripples for $\vartheta > \vartheta_c$. Clearly, neither of the two models alone is able to account for all of our experimental observations shown in Fig. 9(a). This in turn suggests that both erosive or redistributive effects may contribute to $\nu_i(\vartheta)$, with the dominant contribution being ϑ dependent [Fig. 9(d)]. Indeed, at near-normal ion incidence angles, it is obvious that the stabilizing redistributive effect dominates the destabilizing erosive one in the x and y directions ($\nu_i^{redist} > -\nu_i^{eros} > 0$). Likewise, at very grazing ion incidence

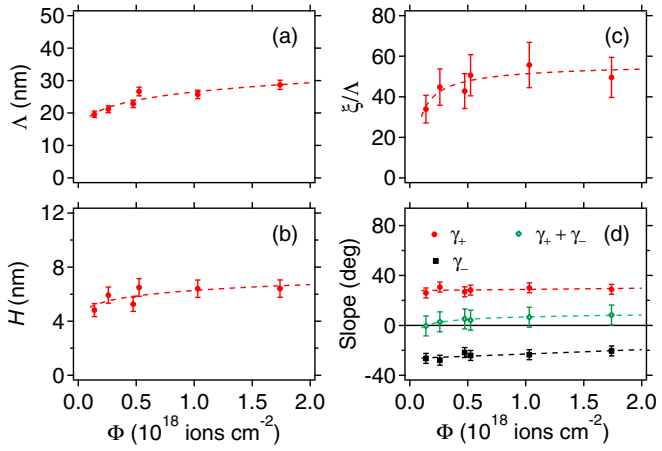

FIG. 8. Morphological variations of nanoripples produced by 1 keV Xe^+ IBS of amorphous alumina thin films as a function of the ion fluence ϕ ($\vartheta = 55^\circ$ and $T = 300$ K): (a) ripple wavelength Λ, (b) ripple height H, (c) normalized lateral correlation length ξ/Λ, and (d) average slope γ_+ (γ_-) of the upwind (downwind) face. Dotted lines are guides to the eye.

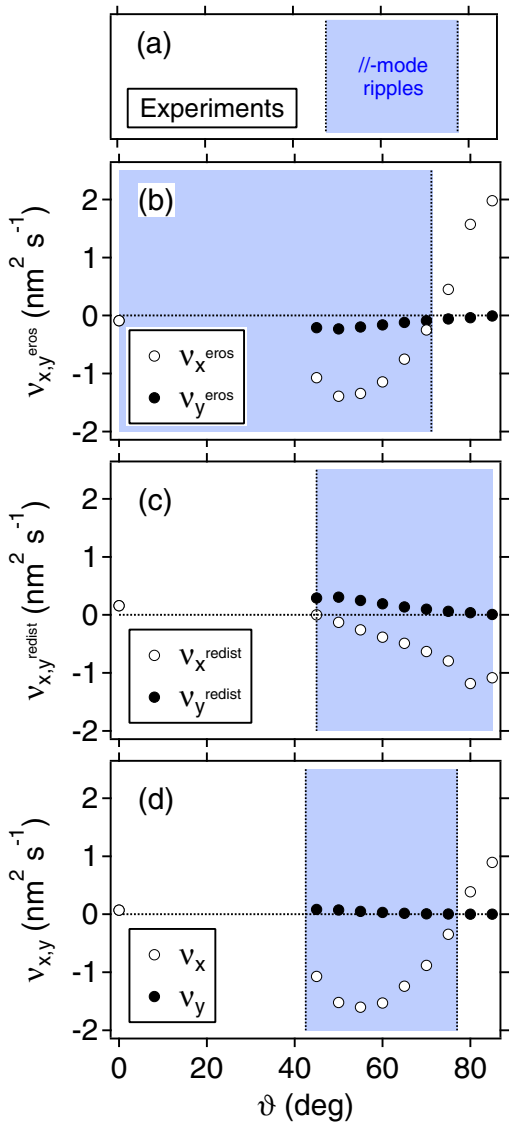

FIG. 9. Surface morphology vs ion incidence angle phase diagrams for 1 keV Xe^+-eroded amorphous alumina thin films at $T = 300$ K. (a) Experimental observations for an erosion time of 340 s. (b) Calculated coefficients ν_x^{eros} and ν_y^{eros}, (c) ν_x^{redist} and ν_y^{redist}, and (d) $\nu_x = \nu_x^{eros} + \nu_x^{redist}$ and $\nu_y = \nu_y^{eros} + \nu_y^{redist}$, as described in the text. The blue shaded areas indicate the angular regions where ripples with wave vector aligned parallel to the projection of the ion beam onto the surface can be expected.

angles, it appears that the stabilizing term is always dominating (i.e., $\nu_x^{eros} > -\nu_x^{redist} > 0$ and $\nu_y^{redist} > -\nu_y^{eros} > 0$), which inhibits the formation of both parallel-mode and perpendicular-mode ripples. Also, combining both erosive and redistributive terms, our calculations (which contain no adjustable parameters) reveal that an instability of the surface leading to the formation of parallel-mode ripples is predicted in the angular range ϑ between 45° and 77°. It is worth noting that the most significant contribution to ripple formation comes from curvature-dependent erosion between 45° and 65°, while ion-induced mass redistribution becomes dominant below $\vartheta = 45°$ and above $\vartheta = 65°$. Overall, the phase diagram prediction displayed in Fig. 9(d) agrees reasonably well with our experimental observations, at least qualitatively recognizing that boundaries between distinct regions are extremely sensitive to small changes in the Sigmund's parameters (a, σ, and μ) or to the occurrence of other competing mechanisms. For example, the inability to predict the emergence of roof-tile structures around $\vartheta = 80°$ might result from nonlocal effects, such as the reflection of a substantial fraction of ions impinging on the downwind faces (Sec. IV B) [67]. Regarding the transition from stability to instability, our experiments show that parallel-mode ripples appear only for $\vartheta > 45°$, whereas $\nu_x(45°) < 0$ from our calculations. The failure to predict precisely the critical angle when ripple formation starts might be due to an overestimated magnitude of the erosive term $\nu_x^{eros}(\vartheta)$ near $\vartheta = 45°$. In fact, for a compound target, it is well established that the situation may be complicated by the preferential sputtering of one of the components. In the case of Al_2O_3 compounds exposed to a uniform 1 keV Xe^+-ion beam, due to the difference in sputtering yield between Al and O, TRIDYN calculations show that a steady state is eventually reached in which the surface composition deviates from the bulk composition. Furthermore, the steady state surface composition varies with the global incidence angle ϑ (see the Supplemental Material, Figs. S5 and S6 [73]). As a consequence, depending on the ϑ value, this could have a non-negligible impact on the collision cascades and in the estimation of the calculated straggling. In addition, the upwind and downwind faces of the ripples should be impacted differently since the ions impinge at different local incidence angles, which may lead to a nontrivial modulation of the chemical composition at the surface. Hence, building on the seminal work of Shenoy *et al.* on the sputtering of alloy surfaces [54], composition-driven patterning mechanisms that are not included in our calculations have been recently recognized as being essential behind the morphological instability and the process dynamics [55,87–89]. Another possible driving field in the process might be due to the buildup of stress that could develop atop the ion-irradiated film as a consequence of the damage (e.g., Xe incorporation, see the Supplemental Material, Figs. S5 and S6 [73]) induced by the collision cascades [56,57]. Such a mechanism appears to have the same $\cos(2\vartheta)$ angle dependence as the ν_x^{redist} term [Eq. (A12)], and hence predicts a transition from flat to rippled surfaces at $\vartheta = 45°$ in accordance with our experimental observations. However, although this additional mechanism may become relevant if sufficient stress accumulates during ion sputtering, it cannot account for the absence of ripples above 80° (Fig. 1).

2. Relaxation mechanism: Effects of thermal diffusion, ion-induced effective surface diffusion, and surface-confined ion-induced viscous flow

The experimental data reported in Sec. III B reveal a weak temperature dependence of the ripple wavelength $\Lambda = \Lambda_x$. This observation suggests that, in addition to (nonthermal) ion-induced effective surface diffusion, thermally activated mechanisms act as a driving force to smooth out amorphous alumina surfaces under Xe^+ IBS. However, in the present situation, one may anticipate a minor effect of thermal diffusion on ripple formation (a decreasing ripple wavelength with ion energy should otherwise be observed). Actually, if

surface self-diffusion is assumed to be the main thermally driven relaxation mechanism, the coefficient $\mathcal{K}$ in Eqs. (1) and (2) is given by [51]

$$\mathcal{K} = \frac{D_0 \Omega^2 \gamma_S \rho}{k_B T} \exp\left(-\frac{\Delta E_{SD}}{k_B T}\right), \quad (3)$$

where D_0 is the surface diffusion constant, Ω is the atomic volume, γ_S is the surface free energy per unit area, ρ is the areal density of diffusing atoms, ΔE_{SD} is the activation energy for surface diffusion, k_B is the Boltzmann constant, and T is the temperature. Taking values provided by Zhou *et al.* for sapphire surfaces [28] ($D_0 = 10^{-8}$ m^2 s^{-1}, $\Omega = 8.51 \times 10^{-30}$ m^3, $\gamma_S = 0.91$ J m^{-2}, $\rho = 10^{13}$ m^{-2}, and $\Delta E_{SD} = 0.72$ eV), the relaxation coefficient is found to increase from $\mathcal{K} \sim 10^{-9}$ nm^4 s^{-1} at $T = 300$ K to $\mathcal{K} \sim 4 \times 10^{-4}$ nm^4 s^{-1} at $T = 573$ K. For comparison, the value of the ion-induced effective smoothing coefficient calculated with Eq. (A3) for $v_0 = 0.356$ nm s^{-1} and $\vartheta = 55^\circ$ is $K_{xx} = 0.32$ nm^4 s^{-1}, so that thermal diffusion can be clearly neglected here. Moreover, using Eq. (2) to determine the corresponding ripple wavelength yields a value of $\Lambda_x \approx 3.8$ nm, which is smaller than the experimentally observed value by a factor of $\sim$7 [Fig. 4(a)]. This result confirms that thermal diffusion associated to ion-induced effective surface diffusion can be excluded as the main relaxation mechanism.

Another relaxation mechanism, in which smoothing occurs by ion-induced viscous relaxation confined to a near-surface region, has been proposed by Umbach *et al.* [12]. In this case the coefficient $\mathcal{K}$ has the form

$$\mathcal{K} = \frac{\gamma_S a^3 F_{eff}}{3\eta_r} = \mathcal{C}\frac{\gamma_S a^3 F_{eff}}{3} E\left[\exp\left(-\frac{\Delta E_{IVF}}{k_B T}\right) + \omega\right], \quad (4)$$

where $1/\eta_r$ is a flux-independent measure of the viscous relaxation per ion, $\mathcal{C}$ is a proportionality factor, E is the ion energy, ΔE_{IVF} is the activation energy for rearrangement of the network, and ω represents the fraction of the ion-induced viscous relaxation that is T independent. Experimental data presented in Fig. 4(a) (i.e., variation of the ripple wavelength with T) were quantitatively analyzed from Eq. (4) by applying a least-square fitting procedure, which yielded $\mathcal{C} = 4.28 \times 10^{-12}$ J^{-2} m^5, $\Delta E_{IVF} = 0.115$ eV, and $\omega = 0.235$. For $T = 300$ K and $E = 1$ keV, the corresponding η_r value is $\eta_r = 5.9 \times 10^{27}$ J m^{-5}, which is of the same order of magnitude as the value of $\eta_r \approx 5 \times 10^{27}$ J m^{-5} derived from the analysis of sapphire surfaces bombarded by 0.6 keV Ar^+ ions after Zhou *et al.* [28]. Furthermore, the large value of $\mathcal{K} = 15.6$ nm^4 s^{-1} obtained using $F_{eff} = 1.54 \times 10^{15}$ ions cm^{-2} s^{-1} in Eq. (4) is a clear indication that surface-confined ion-induced viscous flow dominates over thermal diffusion and ion-induced effective surface diffusion. Thus, as seen in Fig. 4(a), the experimental dependence of the ripple wavelength on T is remarkably well reproduced by a model combining curvature-dependent erosion and surface-confined ion-induced viscous flow as the dominant roughening and smoothing processes, respectively. In order to prove the consistency of this model as well as its ability to predict the dependence of the ripple wavelength for various experimental conditions, the previous fitting parameters were reused to calculate (without any additional adjustable parameter) the expected variations of Λ_x as a function of ϑ and E. The results are displayed in Figs. 3(b) and 6(a), respectively, which show overall good agreement between experimental and calculated values. The main discrepancies, which appear in Fig. 3(b) for $\vartheta \geqslant 70^\circ$, might be attributed to the fact that the data measured at larger ion incidence angles correspond to a latter stage in the (nonlinear) coarsening process [56,90], or to the contribution of reflected ions resulting in an incessant vanishing of smaller facets [27,66,67].

B. Deviations from the linear continuum models and numerical integrations

Although Eq. (1) is able to reproduce the global variations of the ripple wavelength with ion incidence angle, ion energy, and temperature, it cannot account for several features observed in our experiments, like the power-law dependence of the ripple wavelength and height with ion fluence as well as the development of ripples with an asymmetric profile. Such deviations from linear continuum models suggest that the patterning dynamics is controlled by additional effects (e.g., nonlinear contributions, geometric shadowing, reflection of primary ions, etc.) that are not incorporated in Eq. (1).

1. Geometric shadowing and reflection of primary ions

In recent years, the production of ripples with asymmetric profiles has been reported on ion-eroded silicon [42,62–67], glass [12,23,25], sapphire [28], mica [36], and pyrochlore [37] surfaces. In most cases, it has been observed that the ripple profile evolves from a symmetric to an asymmetric one with increasing fluence [12,28,63,67], in accordance with our experiments. However, it should be noted that results are conflicting regarding the sign of $\gamma_+ + \gamma_-$, which appears to be either negative [12,25,28,36,62,64] (i.e., the slope γ_+ facing the ion beam is less steep than the opposite slope γ_-) or positive [23,42,63,66,67] depending on the experimental conditions. In the latter case, which conforms with our experimental observations, shadowing effects are commonly invoked to explain the development of sawtooth-like faceted ripples [65,66,91,92], especially for grazing incidence IBS conditions. Figure 10(a) shows the dependence of the local incidence angles on the upwind face ($\vartheta - \gamma_+$) and downwind face ($\vartheta - \gamma_-$) as a function of the global incidence angle ϑ for nanoripples produced by 1 keV Xe^+ IBS of amorphous alumina thin films at room temperature. In addition, the fluence dependence of the local incidence angles for $\vartheta = 55^\circ$ is displayed in Fig. 10(b). In the ϑ range from 50° to 65°, it can be seen that the local incidence angle on the downwind face increases gradually as expected, but never reaches 90°. Moreover, for $\vartheta = 55^\circ$, the patterning dynamics results in a slight decrease of $\vartheta - \gamma_-$, whereas the local incidence angle on the upwind face remains apparently stable around $\vartheta - \gamma_+ = 26^\circ \pm 2^\circ$. Based on these findings, geometric shadowing appears not to play a decisive role in the development of asymmetric ripples produced by 1 keV Xe^+ erosion of alumina surfaces with $\vartheta \leqslant 65^\circ$.

Recent works revealed that another possible effect that can operate during the formation of ion-induced ripple patterns at off-normal incidence is the so-called Hauffe mechanism [75]. Such a mechanism, which is based on the reflection of primary ions on the downwind faces (leading to a local flux enhancement onto the upwind faces), has been considered to

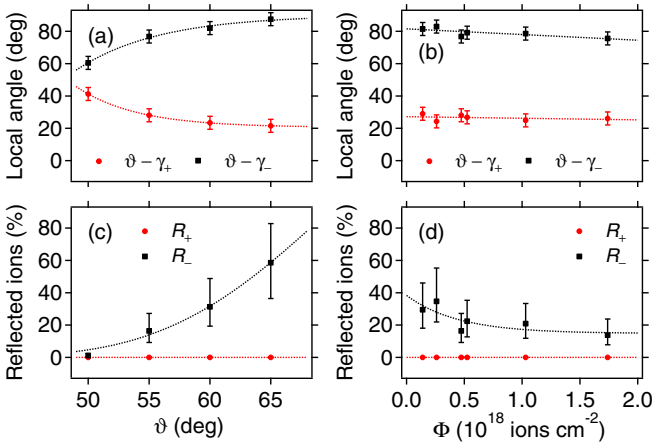

FIG. 10. (a) Variation of the local incidence angles $\vartheta - \gamma_+$ and $\vartheta - \gamma_-$ as a function of the global incidence angle ϑ for nanoripples produced by 1 keV Xe^+ IBS of amorphous alumina thin films during 340 s and (b) as a function of the total fluence ϕ for nanoripples produced by 1 keV Xe^+ IBS of amorphous alumina thin films with $\vartheta = 55^\circ$. (c) and (d) Proportion of reflected ions at the surface layer for the upwind (R_+) and downwind (R_-) ripple faces (based on SRIM [93] calculations).

account for the ripple coarsening observed on ion-eroded Si, Ge, SiO_2, and Al_2O_3 surfaces [23,27,66,67]. Figures 10(c) and 10(d) show the proportion of reflected ions for the upwind (R_+) and downwind (R_-) faces estimated from SRIM [93] calculations. It can be observed that $R_+ \approx 0$ in all experimental conditions, while R_- increases with the global incidence angle and decreases with the total fluence. For comparison, $R_- \approx 0.13$ with $\vartheta = 55^\circ$ and $\phi = 1.74 \times 10^{18}$ ions cm^{-2}, and $R_- \approx 0.59$ with $\vartheta = 65^\circ$ and $\phi = 0.23 \times 10^{18}$ ions cm^{-2}. Accordingly, while the Hauffe mechanism is certainly of minor relevance for $\vartheta \leqslant 55^\circ$, it is very likely that reflected primary ions make a substantial contribution to ripple coarsening and asymmetry in the high ϑ range ($\vartheta \geqslant 65^\circ$). Therefore, this effect might be partly responsible for the observed divergence between the measured and calculated ripple wavelengths in Fig. 3(b), but also for the formation of the roof-tile structure around $\vartheta = 80^\circ$ [67].

2. *Nonlinear contributions to the patterning dynamics*

To investigate the influence of nonlinear effects on the dynamics of ripple formation during room temperature 1 keV Xe^+ IBS of amorphous alumina thin films with $\vartheta = 55^\circ$ and $v_0 = 0.321$ nm s^{-1} (i.e., $F_{\text{eff}} = 1.39 \times 10^{15}$ ions $cm^{-2}\,s^{-1}$), we performed numerical integrations of general continuum equations by considering extensions of the linear Bradley-Harper's theory into the nonlinear regime. According to Makeev *et al.* [52], the time evolution of the surface profile $h(x,y,t)$ can be expressed as

$$\begin{aligned}\frac{\partial h}{\partial t} = &-v_0 + \gamma_x \frac{\partial h}{\partial x} + \nu_x \frac{\partial^2 h}{\partial x^2} + \nu_y \frac{\partial^2 h}{\partial y^2} \\ &- K_{xx} \frac{\partial^4 h}{\partial x^4} - K_{yy} \frac{\partial^4 h}{\partial y^4} - K_{xy} \frac{\partial^2 h}{\partial x^2} \frac{\partial^2 h}{\partial y^2} - \mathcal{K} \nabla^4 h \\ &+ \frac{\lambda_x}{2} \left(\frac{\partial h}{\partial x} \right)^2 + \frac{\lambda_y}{2} \left(\frac{\partial h}{\partial y} \right)^2 + \xi_x \left(\frac{\partial h}{\partial x} \right) \left(\frac{\partial^2 h}{\partial x^2} \right) \\ &+ \xi_y \left(\frac{\partial h}{\partial x} \right) \left(\frac{\partial^2 h}{\partial y^2} \right) + \eta(x,y,t), \end{aligned} \tag{5}$$

where λ_x and λ_y represent the dependence of the erosion rate on the local incidence angle, ξ_x and ξ_y are nonlinearities responsible for the development of ripples with asymmetric profiles, and $\eta(x,y,t)$ is a Gaussian noise term which accounts for the stochastic nature of the IBS process and surface relaxation events. In the framework of Sigmund's theory of ion erosion, the coefficients γ_x, $\nu_i = \nu_i^{\text{eros}} + \nu_i^{\text{redist}}$, K_{ij}, λ_i, and ξ_i in Eq. (5) can be calculated from Eqs. (A1)–(A18) given in the Appendix. The corresponding values estimated for our experimental conditions are tabulated in Table II, indicating that $\lambda_x < \lambda_y < 0$ and $\xi_x < \xi_y < 0$. Furthermore, the ion-induced viscous relaxation coefficient calculated from Eq. (4) with $F_{\text{eff}} = 1.39 \times 10^{15}$ ions $cm^{-2}\,s^{-1}$ is $\mathcal{K} = 14.04$ $nm^4\,s^{-1}$. For these parameters, Eq. (2) yields a periodicity of $\Lambda_x = 26.6$ nm. Equation (5) was integrated numerically using the RIPPLES AND DOTS package written in MATLAB® [94]. A simple finite difference Euler's method with periodic boundary conditions was employed on a 500×500 spatial mesh with a spatial discretization of $\Delta x = \Delta y = 1$ nm and a time step of $\Delta t = 0.001$ s. The noise term was set to $\eta = 0.01$ nm s^{-1} and the AFM image of an as-grown (unsputtered) alumina thin film (Fig. 1) was used as initial surface roughness at time $t = 0$ to provide a realistic initial condition for all simulations. In Fig. 11, simulated images of the surface morphology calculated by integrating Eq. (5) are compared with experimental AFM images of alumina thin films exposed to a uniform 1 keV Xe^+-ion beam with $\vartheta = 55^\circ$ during 100 s ($\phi = 1.39 \times 10^{17}$ ions cm^{-2}), 187 s ($\phi = 2.60 \times 10^{17}$ ions cm^{-2}), 340 s ($\phi = 4.73 \times 10^{17}$ ions cm^{-2}), and 742 s ($\phi = 1.03 \times 10^{18}$ ions cm^{-2}), respectively. Figure 11(b) shows numerical simulations using the coefficients given in Table II except for $\xi_x = \xi_y = 0$. In contrast to Bradley-Harper's simulations leading to an exponential growth of the ripple amplitude (see the Supplemental Material, Fig. S7 [73]), we observe a gradual increase in the surface roughness consistent with the experimental power-law dependence of σ_{rms} with ϕ. However, while irregular wavelike structures clearly appear in the early stage of simulation, grooves are produced instead of ripples owing to the negative sign of the

TABLE II. Linear and nonlinear ion-stimulated erosive coefficients calculated using the relations given in the Appendix [Eqs. (A1)–(A18)] for 1 keV Xe^+ IBS of amorphous alumina thin films with $\vartheta = 55^\circ$ ($F_{\text{eff}} = 1.39 \times 10^{15}$ ions $cm^{-2}\,s^{-1}$).

γ_x (nm s^{-1})	ν_x ($nm^2\,s^{-1}$)	ν_y ($nm^2\,s^{-1}$)	K_{xx} ($nm^4\,s^{-1}$)	K_{yy} ($nm^4\,s^{-1}$)	K_{xy} ($nm^4\,s^{-1}$)	λ_x (nm s^{-1})	λ_y (nm s^{-1})	ξ_x ($nm^2\,s^{-1}$)	ξ_y ($nm^2\,s^{-1}$)
1.57	−1.60	0.051	0.288	0.018	0.242	−3.93	−0.71	−6.86	−0.80

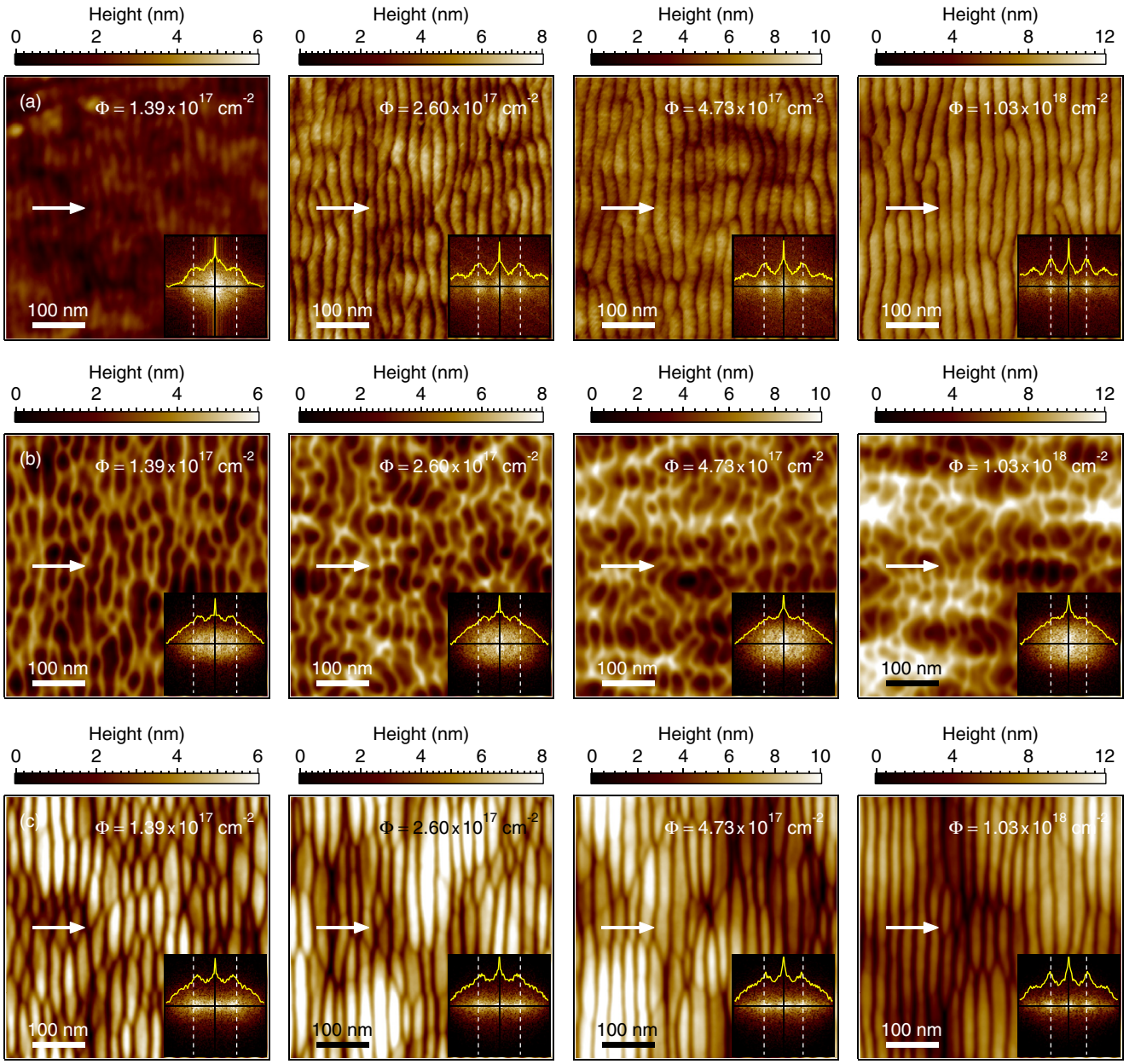

FIG. 11. (a) AFM topographic images of amorphous alumina thin films after 1 keV Xe^+-ion exposure with increasing ion fluences ϕ ($\vartheta = 55^\circ$ and $T = 300$ K). (b) Numerical integration of Eq. (5) using $\mathcal{K} = 14.04$ nm^4 s^{-1} and the coefficients listed in Table II except for $\xi_x = \xi_y = 0$. (c) Numerical integration of Eq. (5) using $\mathcal{K} = 14.04$ nm^4 s^{-1} and the coefficients listed in Table II except for $\lambda_x = 2.6$ nm s^{-1}, $\lambda_y = 10\lambda_x$, and $\xi_x = \xi_y = 0$. Corresponding PSD are shown in the inset together with associated 1D profiles (dotted lines indicate the positions of the *experimental* first-order peaks). The projection of the ion-beam direction onto the surface (x direction) is indicated by the white arrows.

λ_i coefficients [79,95]. Moreover, at longer times, the periodic pattern becomes increasingly blurred and the surface exhibits kinetic roughening as commonly reported when $\lambda_y/\lambda_x \lesssim 1$ [78,96]. Actually, it can be observed in Fig. 11(c) that the dynamics of the surface evolution is strongly affected by the sign of the λ_i coefficients and by the λ_y/λ_x ratio. Indeed, setting $\lambda_x = 2.6$ nm s^{-1} and $\lambda_y/\lambda_x = 10$ not only turns the grooves into disordered ripples at early times, but also transforms the cellularlike structures into ripplelike structures with increasing degree of ordering and homogeneity at higher fluences. Hence, while the results from the above confirm that the dynamics of ripple formation is dominated by nonlinear effects, it appears that in addition to the nonlinear terms calculated by applying Sigmund's theory, other nonlinear effects due to, e.g., redeposition [97], surface stress [56,57,82], or coupling between the surface topography and the surface transport [53,79] or composition [54,55] should also be considered.

3. *Nonlinear contributions to the profile asymmetry*

Since the numerical simulation presented in Fig. 11(c) was performed with $\xi_x = \xi_y = 0$, it is not able to reproduce the asymmetric profile of the ripples. This is clearly evidenced in Fig. 12(a), showing the evolution of the slope angle

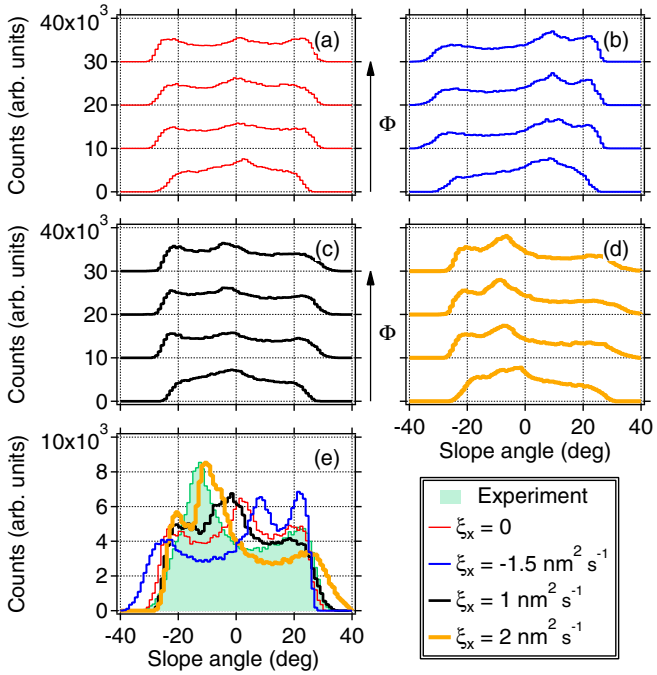

FIG. 12. (a) Slope angle distributions obtained at $\phi = 1.39 \times 10^{17}$ ions cm^{-2}, $\phi = 2.60 \times 10^{17}$ ions cm^{-2}, $\phi = 4.73 \times 10^{17}$ ions cm^{-2}, and $\phi = 1.03 \times 10^{18}$ ions cm^{-2} from the numerical simulations presented in Fig. 11(c) with $\xi_x = \xi_y = 0$. Slope angle distributions obtained from numerical simulations with (b) $\xi_x = -1.5$ nm^2 s^{-1}, (c) $\xi_x = 1$ nm^2 s^{-1}, and (d) $\xi_x = 2$ nm^2 s^{-1}. (e) Slope angle distributions obtained from numerical simulations and from AFM observation of an alumina thin film after room temperature 1 keV Xe$^+$-ion exposure with $\vartheta = 55^\circ$ and $\phi = 1.75 \times 10^{18}$ ions cm^{-2}.

distribution with ion fluence when the nonlinear terms of the form $(\partial h/\partial x)(\partial^2 h/\partial i^2)$ are not considered in the simulation. In contrast, with $\xi_x = -1.5$ nm^2 s^{-1}, the surface develops asymmetric ripples with the (positive) slope facing the ion beam being less steep than the opposite (negative) slope [Fig. 12(b)], which contradicts our experimental observations. Instead, for positive values of ξ_x, the patterning dynamics results in the development of ripples with the slope of the upwind face increasing more rapidly than the slope of the downwind face [Figs. 12(c) and 12(d)]. So, as seen in Fig. 12(e), the slope angle distribution obtained by numerical simulation at $t = 1256$ s with $\xi_x = 2$ nm^2 s^{-1} compares reasonably well with that determined by AFM from a 1 keV Xe$^+$-eroded amorphous alumina thin film with $\vartheta = 55^\circ$ and $\phi = 1.75 \times 10^{18}$ ions cm^{-2}. This tends to confirm that the nonlinear coefficients given in Table II are not correctly estimated, and therefore suggests that additional nonlinear effects that are not captured by the Sigmund's theory contribute to the formation of the ripple pattern.

4. Nonlinear contributions to the wavelength coarsening

Although the numerical integration of Eq. (5) can provide a successful description of the evolution of the ripple profile, it fails to reproduce the coarsening of the ripple wavelength with fluence clearly seen in the experiments [Figs. 8(a) and 11(a)]. Indeed, the PSD analysis of the images displayed in Fig. 11(c) (insets) reveals that the evolution of the ripple wavelength is not correctly reproduced by the simulation, especially at low fluences $\phi \leqslant 2.60 \times 10^{17}$ ions cm^{-2}. In the last decade, to overcome the inability of single-field models to predict ripple coarsening, coupled two-field models have been proposed to describe the evolution of surfaces subjected to IBS at off-normal incidence [53–55,79]. Following the theory introduced by Muñoz-García *et al.* [53,79], in which the surface topography is coupled to the thickness of a mobile layer, the surface height evolution $h(x,y,t)$ of an amorphous solid can then be described by

$$\begin{aligned}\frac{\partial h}{\partial t} = &-v_0 + \gamma_x \frac{\partial h}{\partial x} + \nu_x \frac{\partial^2 h}{\partial x^2} + \nu_y \frac{\partial^2 h}{\partial y^2} - K_{xx} \frac{\partial^4 h}{\partial x^4} \\ &- K_{yy} \frac{\partial^4 h}{\partial y^4} - K_{xy} \frac{\partial^2 h}{\partial x^2} \frac{\partial^2 h}{\partial y^2} - \mathcal{K} \nabla^4 h \\ &+ \frac{\lambda_x}{2} \left(\frac{\partial h}{\partial x} \right)^2 + \frac{\lambda_y}{2} \left(\frac{\partial h}{\partial y} \right)^2 - \lambda_x^{(2)} \frac{\partial^2}{\partial x^2} \left(\frac{\partial h}{\partial x} \right)^2 \\ &- \lambda_y^{(2)} \frac{\partial^2}{\partial y^2} \left(\frac{\partial h}{\partial y} \right)^2 + \eta(x,y,t), \end{aligned} \tag{6}$$

where $\lambda_i^{(2)}$ are positive coefficients, which physically reflect local redeposition of sputtered material and surface-confined transport. For the sake of simplicity, the nonlinear terms of the form $(\partial h/\partial x)(\partial^2 h/\partial i^2)$ are not considered in Eq. (6) because they do not contribute to the evolution of the ripple wavelength with time. In contrast, in comparison with Eq. (5), the further presence of the nonlinear $\lambda_x^{(2)}$ coefficient in Eq. (6) tends to promote coarsening of the ripple wavelength, especially for large $\lambda_x^{(2)}/\lambda_x$ values [79]. In order to stress the importance of this additional nonlinearity, simulation of alumina surface evolution during 1 keV Xe$^+$ IBS with $\vartheta = 55^\circ$ was performed by numerical integration of Eq. (6). Figure 13 shows snapshots of the simulated surface morphology for integration times $t = 100$ to 742 s using the following parameters: $\mathcal{K} = 5$ nm^4 s^{-1}, $\lambda_x = 0.6$ nm s^{-1}, $\lambda_y = 6$ nm s^{-1}, $\lambda_x^{(2)} = 10$ nm^3 s^{-1}, and $\lambda_y^{(2)} = 0$. It is seen that the surface morphology evolves in a manner reasonably consistent with experimental observations shown in Fig. 11(a). Specifically, not only the power-law dependence of the ripple wavelength and height but also the progressive enhancement of pattern ordering with time are reproduced by the simulation (see insets in Fig. 13 and the Supplemental Material, Fig. S8 [73]). Although more refined models that have been demonstrated to lead to a narrow band of unstable wavelengths in the case of binary compounds (e.g., ion-assisted phase separation [87,88] or coupling between the topography of the surface and a thin surface layer of altered composition [54,55]) could also be considered, the relative agreement between experiments and numerical simulations reflects that the formation of periodic nanoripples by IBS of amorphous alumina surfaces arises as the complex interplay between multiple physical mechanisms, which extend well beyond Sigmund's theory.

V. CONCLUSION

The morphological evolution of amorphous alumina surfaces under low-energy Xe$^+$ IBS has been investigated in detail by *ex situ* AFM and 3D GISAXS reciprocal

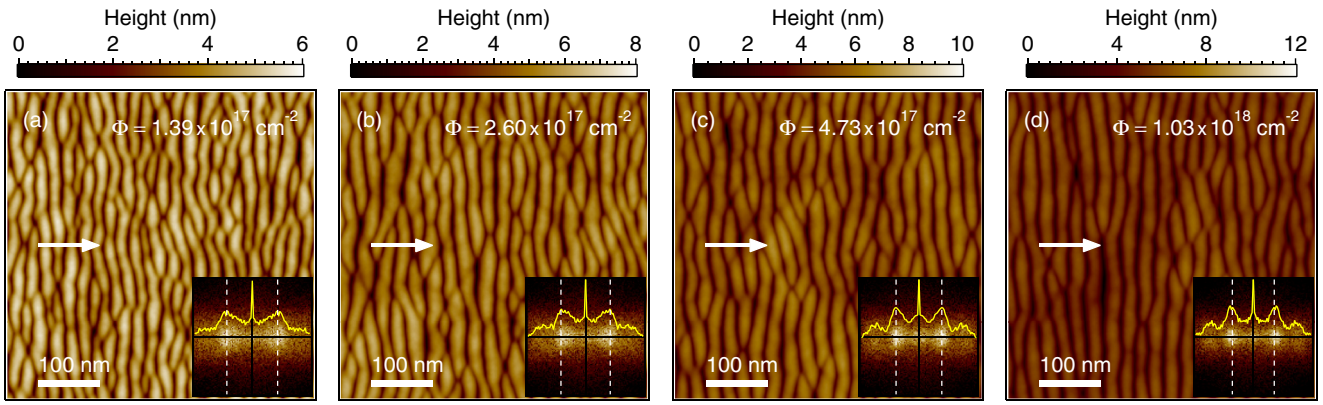

FIG. 13. Numerical integration of Eq. (6) using $\mathcal{K} = 5$ nm^4 s^{-1} and the coefficients listed in Table II except for $\lambda_x = 0.6$ nm s^{-1}, $\lambda_y = 6$ nm s^{-1}, $\lambda_x^{(2)} = 10$ nm^3 s^{-1}, and $\lambda_y^{(2)} = 0$. (a) Integration time $t = 100$ s, (b) $t = 187$ s, (c) $t = 340$ s, and (d) $t = 742$ s. Corresponding PSD are shown in the inset together with associated 1D profiles [dotted lines indicate the positions of the *experimental* first-order peaks, see Fig. 11(a)]. The projection of the ion-beam direction onto the surface (x direction) is indicated by the white arrows.

space mapping. It is shown that periodic nanoripples oriented perpendicular to the projection of the ion beam onto the surface develop for ion incidence angles ranging between $\vartheta = 50°$ and 75°. In contrast, the surface remains smooth for $\vartheta \leqslant 45°$ and $\vartheta \geqslant 85°$, while roof-tile structures elongated along the ion beam emerge for $\vartheta \approx 80°$. Our experiments show that the ripple wavelength of patterns produced with $\vartheta = 55°$ increases with temperature, ion energy, and fluence, whereas the pattern ordering is enhanced with ion fluence, but deteriorates with increasing temperature. Moreover, ripple patterns present an asymmetric profile which is all the more pronounced that the ion incidence angle is large or erosion duration is long. The observed dependence of the surface morphology on ion incidence angle, temperature, and ion energy has been discussed in the framework of linear continuum theoretical models. The ensemble of our results allow us to conclude that the physical processes involved in the morphological evolution of ion-eroded alumina surfaces include both erosive or redistributive effects. However, while mass redistribution acts as a driving force to smoothen the surface at near-normal and very grazing incidence angles, an instability mechanism by curvature-dependent erosion dominates the formation of ripple patterns in the ϑ range from 50° to 65°. Furthermore, regarding the possible relaxation mechanisms, it appears clear that surface-confined ion-induced viscous flow dominates over thermal diffusion and ion-induced effective surface diffusion. Our results also suggest that geometric shadowing and reflection of primary ions may have only a minor impact on patterning for ion incidence angles below 65°, while playing a substantial role for ripple coarsening and asymmetry in the high ϑ range. Although our linear model is successful in predicting the dependence of ripple wavelength with ion incidence angle, temperature, and ion energy, pattern evolution with ion fluence also reveals that nonlinear effects contribute strongly to the dynamics of ripple formation. However, comparison of the observed patterning dynamics to numerical integrations of nonlinear differential equations show that complex nonlinear effects, such as local redeposition or surface-confined transport, might control the time evolution of the ripple wavelength and profile (height and asymmetry). Beyond the theoretical improvements still needed for progress towards the quantitative continuum description of the present experiments, it is nevertheless worth noting that IBS allows us to control the morphology of rippled alumina surfaces that might be used as efficient templates to tailor electrical, optical or magnetic properties of functional thin films or nanostructures [18,50].

ACKNOWLEDGMENTS

This work has been carried out within the QMAX Project No. ANR-09-NANO-031 funded by the French National Agency (ANR) in the frame of its 2009 programme in Nanosciences, Nanotechnologies and Nanosystems (P3N2009). We acknowledge the ESRF and the French Collaborating Research Group (CRG) for provision of synchrotron radiation facilities. The authors are particularly grateful to the staff members of D2AM (CRG-BM02) and to M. Maret (Laboratoire de Science et Ingénierie des Matériaux et Procédés, Grenoble-INP/CNRS/UJF) for assistance in using the beamline. We would like to express our deepest gratitude to S. Facsko (Institute of Ion Beam Physics and Materials Research, Helmholtz-Zentrum Dresden-Rossendorf) for providing us with the RIPPLES AND DOTS package and for fruitful discussions on ion-induced pattern formation. We also thank P. Guérin (Institut Pprime, CNRS/Université de Poitiers) for assistance during the sample preparation.

APPENDIX

Linear ion-stimulated erosive coefficients in Eq. (1) can be calculated using the relations given by Bradley [98]:

$$\gamma_x = \frac{v_0}{\cos\vartheta}\frac{\sin\vartheta}{B_1^2}\left[\frac{a^2}{\sigma^2}\frac{a^2}{\mu^2}\left(\frac{a^2}{\sigma^2}-1\right)\cos^2\vartheta - A^2\right], \tag{A1}$$

$$\nu_i^{\text{eros}} = \frac{v_0}{\cos\vartheta} a\Gamma_i, \tag{A2}$$

$$K_{\text{xx}} = \frac{v_0}{\cos\vartheta}\frac{a^2}{\sigma^2}\frac{a^3}{24B_1^5}\left[\frac{a^2}{\mu^2}\left(3B_1^2 + 6B_1\frac{a^4}{\sigma^4}\sin^2\vartheta + \frac{a^8}{\sigma^8}\sin^4\vartheta\right)\cos^2\vartheta - 4\frac{a^2}{\sigma^2}\left(3B_1 + \frac{a^4}{\sigma^4}\sin^2\vartheta\right)\sin^2\vartheta\right]\cos^2\vartheta, \tag{A3}$$

$$K_{\text{yy}} = \frac{v_0}{\cos\vartheta}\frac{a^3}{8B_1}\frac{\mu^2}{\sigma^2}\cos^2\vartheta, \tag{A4}$$

$$K_{\text{xy}} = -\frac{1}{2}\mu^2\nu_{\text{x}}, \tag{A5}$$

with

$$\Gamma_{\text{x}} = \frac{A}{B_1}\sin\vartheta - \frac{B_2}{2B_1}\left(1 + \frac{A^2}{B_1}\right)\cos\vartheta - \frac{AC}{B_1^2}\left(3 + \frac{A^2}{B_1}\right)\cos\vartheta, \tag{A6}$$

$$\Gamma_{\text{y}} = -\frac{a^2}{\sigma^2}\frac{\cos^2\vartheta}{2B_1}, \tag{A7}$$

and

$$A = \frac{a^2}{\sigma^2}\sin\vartheta, \tag{A8}$$

$$B_1 = \frac{a^2}{\sigma^2}\sin^2\vartheta + \frac{a^2}{\mu^2}\cos^2\vartheta, \tag{A9}$$

$$B_2 = \frac{a^2}{\sigma^2}\cos\vartheta, \tag{A10}$$

$$C = \frac{1}{2}\left(\frac{a^2}{\mu^2} - \frac{a^2}{\sigma^2}\right)\cos\vartheta\sin\vartheta. \tag{A11}$$

Furthermore, the redistributive contribution of the curvature-dependent coefficients can be calculated using the relations given by Davidovitch *et al.* [59] after the seminal work of Carter and Vishnyakov [58]:

$$\nu_{\text{x}}^{\text{redist}} = F_{\text{eff}}\Omega\frac{\delta}{2}\cos 2\vartheta = \frac{v_0}{\cos\vartheta}\frac{a}{2}\cos 2\vartheta, \tag{A12}$$

$$\nu_{\text{y}}^{\text{redist}} = F_{\text{eff}}\Omega\frac{\delta}{2}\cos^2\vartheta = v_0\frac{a}{2}\cos\vartheta, \tag{A13}$$

assuming that the sum δ of atomic shifts (recoil atoms) generated by each incident ion is

$$\delta \approx Y_0(\vartheta)a = \frac{v_0}{F_{\text{eff}}\Omega\cos\vartheta}a. \tag{A14}$$

Lastly, nonlinear coefficients in Eq. (5) can also be calculated using the relations given by Makeev *et al.* [52]:

$$\lambda_{\text{x}} = \frac{v_0}{2B_1^4}\left\{A^4\frac{a^2}{\mu^2}(3 + 2\cos^2\vartheta) + 4\frac{a^6}{\sigma^6}\frac{a^4}{\mu^4}\sin^2\vartheta\cos^4\vartheta - \frac{a^4}{\sigma^4}\frac{a^6}{\mu^6}\cos^4\vartheta(1 + 2\sin^2\vartheta)\right.$$
$$\left. - B_1^2\left[2A^2 - \frac{a^2}{\sigma^2}\frac{a^2}{\mu^2}(1 + 2\sin^2\vartheta)\right] - \frac{a^8}{\sigma^8}\frac{a^4}{\mu^4}\sin^2\vartheta\cos^2\vartheta - B_1^4\right\}, \tag{A15}$$

$$\lambda_{\text{y}} = \frac{v_0}{2B_1^2}\left(A^2 + \frac{a^2}{\sigma^2}\frac{a^2}{\mu^2}\cos^2\vartheta - B_2^2\frac{a^2}{\mu^2} - B_1^2\right), \tag{A16}$$

$$\xi_{\text{x}} = \frac{v_0}{2B_1^5}\frac{a^3\sin\vartheta}{\sigma^2}\left[-6\frac{a^8}{\sigma^8}\sin^6\vartheta + A^4\frac{a^2}{\mu^2}(4 + 3\cos^2\vartheta) - \frac{a^8}{\sigma^8}\frac{a^4}{\mu^4}\cos^2\vartheta\sin^2\vartheta + \frac{a^6}{\sigma^6}\frac{a^4}{\mu^4}\cos^2\vartheta\sin^2\vartheta(4 - 6\sin^2\vartheta)\right.$$
$$+ \frac{a^6}{\sigma^6}\frac{a^2}{\mu^2}\sin^4\vartheta(-3 + 15\sin^2\vartheta) + 3\frac{a^4}{\sigma^4}\frac{a^4}{\mu^4}\cos^2\vartheta\sin^2\vartheta(4 + 3\sin^2\vartheta) - 3\frac{a^4}{\sigma^4}\frac{a^6}{\mu^6}\cos^4\vartheta(1 + \sin^2\vartheta)$$
$$\left. + \frac{a^2}{\sigma^2}\frac{a^6}{\mu^6}\cos^4\vartheta(9 - 3\sin^2\vartheta) - 3\frac{a^8}{\mu^8}\cos^6\vartheta\right], \tag{A17}$$

$$\xi_{\text{y}} = \frac{v_0}{2B_1^3}\frac{a^3\sin\vartheta}{\sigma^2}\left[-\frac{a^4}{\sigma^4}\frac{a^2}{\mu^2}\cos^2\vartheta + \frac{a^4}{\sigma^4}\sin^2\vartheta(2 + \cos^2\vartheta) - \frac{a^4}{\mu^4}\cos^4\vartheta + \frac{a^2}{\sigma^2}\frac{a^2}{\mu^2}\cos^2\vartheta(3 - 2\sin^2\vartheta)\right]. \tag{A18}$$

[1] U. Valbusa, C. Boragno, and F. Buatier de Mongeot, J. Phys.: Condens. Matter **14**, 8153 (2002).
[2] W. L. Chan and E. Chason, J. Appl. Phys. **101**, 121301 (2007).
[3] J. Muñoz-García, L. Vásquez, R. Cuerno, J. A. Sánchez-García, M. Castro, and R. Gago, *Towards Functional Nanomaterials*, edited by Z. M. Wang (Springer, New York, 2009), pp. 323–398.
[4] D. Ghose, J. Phys.: Condens. Matter **21**, 224001 (2009).
[5] E. Chason, T. M. Mayer, B. K. Kellerman, D. T. McIlroy, and A. J. Howard, Phys. Rev. Lett. **72**, 3040 (1994).
[6] S. Facsko, T. Dekorsy, C. Koerdt, C. Trappe, H. Kurz, A. Vogt, and H. L. Hartnagel, Science **285**, 1551 (1999).
[7] M. Szymonski, F. Krok, P. Struski, J. Kolodziej, and B. Such, Prog. Surf. Sci. **74**, 331 (2003).
[8] O. Plantevin, R. Gago, L. Vázquez, A. Biermanns, and T. H. Metzger, Appl. Phys. Lett. **91**, 113105 (2007).
[9] D. Carbone, A. Biermanns, B. Ziberi, F. Frost, O. Plantevin, U. Pietsch, and T. H. Metzger, J. Phys.: Condens. Matter **21**, 224007 (2009).
[10] J. Muñoz-García, L. Vázquez, M. Castro, R. Gago, A. Redondo-Cubero, A. Moreno-Barrado, and R. Cuerno, Mater. Sci. Eng. R **86**, 1 (2014).
[11] T. M. Mayer, E. Chason, and A. J. Howard, J. Appl. Phys. **76**, 1633 (1994).
[12] C. C. Umbach, R. L. Headrick, and K.-C. Chang, Phys. Rev. Lett. **87**, 246104 (2001).
[13] P. F. A. Alkemade, Phys. Rev. Lett. **96**, 107602 (2006).
[14] A. Keller, S. Facsko, and W. Möller, J. Phys.: Condens. Matter **21**, 495305 (2009).
[15] A. Keller, S. Facsko, and W. Möller, Nucl. Instrum. Methods Phys. Res. B **267**, 656 (2009).
[16] S. Camelio, D. Babonneau, D. Lantiat, L. Simonot, and F. Pailloux, Phys. Rev. B **80**, 155434 (2009).
[17] D. Babonneau, S. Camelio, E. Vandenhecke, S. Rousselet, M. Garel, F. Pailloux, and P. Boesecke, Phys. Rev. B **85**, 235415 (2012).
[18] S. Camelio, E. Vandenhecke, S. Rousselet, and D. Babonneau, Nanotechnology **25**, 035706 (2014).
[19] H. X. Qian and W. Zhou, J. Phys. D: Appl. Phys. **42**, 105304 (2009).
[20] D. Flamm, F. Frost, and D. Hirsch, Appl. Surf. Sci. **179**, 95 (2001).
[21] A. Toma, F. Buatier de Mongeot, R. Buzio, G. Firpo, S. Bhattacharyya, C. Boragno, and U. Valbusa, Nucl. Instrum. Methods Phys. Res. B **230**, 551 (2005).
[22] A. Toma, D. Chiappe, D. Massabò, C. Boragno, and F. Buatier de Mongeot, Appl. Phys. Lett. **93**, 163104 (2008).
[23] J. Völlner, B. Ziberi, F. Frost, and B. Rauschenbach, J. Appl. Phys. **109**, 043501 (2011).
[24] S. A. Khan, D. K. Avasthi, D. C. Agarwal, U. B. Singh, and D. Kabiraj, Nanotechnology **22**, 235305 (2011).
[25] H. Gnaser, B. Reuscher, and A. Zeuner, Nucl. Instrum. Methods Phys. Res. B **285**, 142 (2012).
[26] D. Kramczynski, B. Reuscher, and H. Gnaser, Phys. Rev. B **89**, 205422 (2014).
[27] M. Teichmann, J. Lorbeer, F. Frost, and B. Rauschenbach, Nanoscale Res. Lett. **9**, 439 (2014).
[28] H. Zhou, Y. Wang, L. Zhou, R. L. Headrick, A. S. Özcan, Y. Wang, G. Özaydin, K. F. Ludwig, Jr., and D. P. Siddons, Phys. Rev. B **75**, 155416 (2007).
[29] H. Zhou, L. Zhou, G. Özaydin, K. F. Ludwig, and R. L. Headrick, Phys. Rev. B **78**, 165404 (2008).
[30] T. Luttrell, W.-K. Li, X.-Q. Gong, and M. Batzill, Phys. Rev. Lett. **102**, 166103 (2009).
[31] M. Kolmer, A. A. Zebari, M. Goryl, F. Buatier de Mongeot, F. Zasada, W. Piskorz, P. Pietrzyk, Z. Sojka, F. Krok, and M. Szymonski, Phys. Rev. B **88**, 195427 (2013).
[32] V. Mussi, F. Granone, C. Boragno, F. Buatier de Mongeot, U. Valbusa, T. Marolo, and R. M. Montereali, Appl. Phys. Lett. **88**, 103116 (2006).
[33] F. Krok, S. R. Saeed, Z. Postawa, and M. Szymonski, Phys. Rev. B **79**, 235432 (2009).
[34] S. Habenicht, W. Bolse, K. P. Lieb, K. Reimann, and U. Geyer, Phys. Rev. B **60**, R2200 (1999).
[35] O. Bobes, K. Zhang, and H. Hofsäss, Phys. Rev. B **86**, 235414 (2012).
[36] A. Metya, D. Ghose, S. A. Mollick, and A. Majumdar, J. Appl. Phys. **111**, 074306 (2012).
[37] Q. Wei, J. Lian, L. A. Boatner, L. M. Wang, and R. C. Ewing, Phys. Rev. B **80**, 085413 (2009).
[38] Q. Wei, J. Lian, S. Zhu, W. Li, K. Sun, and L. Wang, Chem. Phys. Lett. **452**, 124 (2008).
[39] M. Goyal, S. Aggarwal, and A. Sharma, J. Appl. Phys. **119**, 115303 (2016).
[40] T. W. H. Oates, A. Keller, S. Facsko, and A. Mücklich, Plasmonics **2**, 47 (2007).
[41] D. Babonneau, S. Camelio, L. Simonot, F. Pailloux, P. Guérin, B. Lamongie, and O. Lyon, Europhys. Lett. **93**, 26005 (2011).
[42] M. Ranjan and S. Facsko, Nanotechnology **23**, 485307 (2012).
[43] D. Gkogkou, B. Schreiber, T. Shaykhutdinov, H. K. Ly, U. Kuhlmann, U. Gernert, S. Facsko, P. Hildebrandt, N. Esser, K. Hinrichs, I. M. Weidinger, and T. W. H. Oates, ACS Sensors **1**, 318 (2016).
[44] Y. J. Chen, J. P. Wang, E. W. Soo, L. Wu, and T. C. Chong, J. Appl. Phys. **91**, 7323 (2002).
[45] F. Bisio, R. Moroni, F. Buatier de Mongeot, M. Canepa, and L. Mattera, Phys. Rev. Lett. **96**, 057204 (2006).
[46] M. O. Liedke, B. Liedke, A. Keller, B. Hillebrands, A. Mücklich, S. Facsko, and J. Fassbender, Phys. Rev. B **75**, 220407 (2007).
[47] M. Körner, K. Lenz, M. O. Liedke, T. Strache, A. Mücklich, A. Keller, S. Facsko, and J. Fassbender, Phys. Rev. B **80**, 214401 (2009).
[48] K. V. Sarathlal, D. Kumar, and A. Gupta, Appl. Phys. Lett. **98**, 123111 (2011).
[49] K. Chen, R. Frömter, S. Rössler, N. Mikuszeit, and H. P. Oepen, Phys. Rev. B **86**, 064432 (2012).
[50] M. Garel, D. Babonneau, A. Boulle, F. Pailloux, A. Coati, Y. Garreau, A. Y. Ramos, and H. C. N. Tolentino, Nanoscale **7**, 1437 (2015).
[51] R. M. Bradley and J. M. E. Harper, J. Vac. Sci. Technol. A **6**, 2390 (1988).
[52] M. A. Makeev, R. Cuerno, and A.-L. Barabási, Nucl. Instrum. Methods Phys. Res. B **197**, 185 (2002).
[53] J. Muñoz-García, R. Cuerno, and M. Castro, Phys. Rev. B **78**, 205408 (2008).
[54] V. B. Shenoy, W. L. Chan, and E. Chason, Phys. Rev. Lett. **98**, 256101 (2007).
[55] F. C. Motta, P. D. Shipman, and R. M. Bradley, Phys. Rev. B **90**, 085428 (2014).

[56] M. Castro, R. Gago, L. Vázquez, J. Muñoz-García, and R. Cuerno, Phys. Rev. B **86**, 214107 (2012).
[57] S. A. Norris, Phys. Rev. B **86**, 235405 (2012).
[58] G. Carter and V. Vishnyakov, Phys. Rev. B **54**, 17647 (1996).
[59] B. Davidovitch, M. J. Aziz, and M. P. Brenner, Phys. Rev. B **76**, 205420 (2007).
[60] C. S. Madi, E. Anzenberg, K. F. Ludwig, and M. J. Aziz, Phys. Rev. Lett. **106**, 066101 (2011).
[61] S. A. Norris, J. Samela, L. Bukonte, M. Backman, F. Djurabekova, K. Nordlund, C. S. Madi, M. P. Brenner, and M. J. Aziz, Nat. Commun. **2**, 276 (2011).
[62] Y. Homma, A. Takano, and Y. Higashi, Appl. Surf. Sci. **203-204**, 35 (2003).
[63] D. P. Datta and T. K. Chini, Phys. Rev. B **69**, 235313 (2004).
[64] B. Ziberi, F. Frost, T. Höche, and B. Rauschenbach, Phys. Rev. B **72**, 235310 (2005).
[65] A. Redondo-Cubero, R. Gago, F. J. Palomares, A. Mücklich, M. Vinnichenko, and L. Vázquez, Phys. Rev. B **86**, 085436 (2012).
[66] T. Basu, D. P. Datta, and T. Som, Nanoscale Res. Lett. **8**, 289 (2013).
[67] M. Engler, S. Macko, F. Frost, and T. Michely, Phys. Rev. B **89**, 245412 (2014).
[68] W. Möller, W. Eckstein, and J. P. Biersack, Comput. Phys. Commun. **51**, 355 (1988).
[69] J. P. Biersack, Z. Phys. A **305**, 95 (1982).
[70] D. Babonneau, S. Camelio, E. Vandenhecke, S. Rousselet, M. Garel, F. Pailloux, and P. Boesecke, Phys. Rev. B **87**, 159903(E) (2013).
[71] D. Babonneau, J. Appl. Crystallogr. **43**, 929 (2010).
[72] E. Anzenberg, C. S. Madi, M. J. Aziz, and K. F. Ludwig, Phys. Rev. B **84**, 214108 (2011).
[73] See Supplemental Material at http://link.aps.org/supplemental/10.1103/PhysRevB.95.085412 for supplementary analyses and simulations.
[74] M. Teichmann, J. Lorbeer, B. Ziberi, F. Frost, and B. Rauschenbach, New J. Phys. **15**, 103029 (2013).
[75] W. Hauffe, Phys. Status Solidi A **35**, K93 (1976).
[76] R. Cuerno and A.-L. Barabási, Phys. Rev. Lett. **74**, 4746 (1995).
[77] M. A. Makeev and A.-L. Barabási, Appl. Phys. Lett. **71**, 2800 (1997).
[78] S. Park, B. Kahng, H. Jeong, and A.-L. Barabási, Phys. Rev. Lett. **83**, 3486 (1999).
[79] J. Muñoz-García, M. Castro, and R. Cuerno, Phys. Rev. Lett. **96**, 086101 (2006).
[80] G. Carter, Surf. Interface Anal. **25**, 952 (1997).
[81] N. V. Medhekar, W. L. Chan, V. B. Shenoy, and E. Chason, J. Phys.: Condens. Matter **21**, 224021 (2009).
[82] A. Moreno-Barrado, M. Castro, R. Gago, L. Vázquez, J. Muñoz-García, A. Redondo-Cubero, B. Galiana, C. Ballesteros, and R. Cuerno, Phys. Rev. B **91**, 155303 (2015).
[83] G. Ozaydin, K. F. Ludwig, Jr., H. Zhou, and R. L. Headrick, J. Vac. Sci. Technol. B **26**, 551 (2008).
[84] J. Zhou and M. Lu, Phys. Rev. B **82**, 125404 (2010).
[85] H. Hofsäss, Appl. Phys. A **114**, 401 (2014).
[86] W. W. Mullins, J. Appl. Phys. **28**, 333 (1957).
[87] G. Abrasonis and K. Morawetz, Phys. Rev. B **86**, 085452 (2012).
[88] S. A. Norris, J. Appl. Phys. **114**, 204303 (2013).
[89] S. Le Roy, E. Søndergård, I. S. Nerbø, M. Kildemo, and M. Plapp, Phys. Rev. B **81**, 161401 (2010).
[90] T. Basu and T. Som, Appl. Surf. Sci. **310**, 142 (2014).
[91] G. Carter, J. Appl. Phys. **85**, 455 (1999).
[92] D. P. Datta and T. K. Chini, Phys. Rev. B **76**, 075323 (2007).
[93] J. F. Ziegler, J. P. Biersack, and U. Littmark, *The Stopping and Range of Ions in Solids* (Pergamon, New York, 1985).
[94] A. Keller, S. Facsko, and R. Cuerno, *Computational Nanotechnology: Modeling and Applications with MATLAB®*, edited by S. M. Musa (CRC, Boca Raton, FL, 2012), pp. 189–215.
[95] B. Kahng, H. Jeong, and A.-L. Barabási, Appl. Phys. Lett. **78**, 805 (2001).
[96] A. Keller, M. Nicoli, S. Facsko, and R. Cuerno, Phys. Rev. E **84**, 015202 (2011).
[97] R. M. Bradley, Phys. Rev. B **83**, 075404 (2011).
[98] R. M. Bradley, Phys. Rev. B **84**, 075413 (2011).